Computers and Fluids 233 (2022) 105250

Contents lists available at ScienceDirect

Computers and Fluids

journal homepage: www.elsevier.com/locate/compfluid

An efficient Ghost Fluid Method to remove overheating from material interfaces in compressible multi-medium flows

Pedram Bigdelou, Chen Liu, Prashant Tarey, Praveen Ramaprabhu *

Department of Mechanical Engineering and Engineering Science, University of North Carolina at Charlotte, Charlotte, NC 28223–0001, USA

ARTICLE INFO

Keywords:
Ghost Fluid Method (GFM)
Overheating
Multi-medium Riemann problem
Compressible multi-medium flows
Isentropic fix
Surface tension

ABSTRACT

The Ghost Fluid Method (GFM) and its derivatives represent powerful techniques in the numerical simulation of compressible, multi-medium flows, but are nonetheless afflicted by so-called overheating errors at and near material interfaces. These errors take the form of local overshoots and undershoots, and cause the numerical solution to deviate from the exact solution. Overheating errors are commonly addressed by an isobaric fix (or an isentropic fix), where the values at the cells next to the fluid interface are corrected to reduce the numerical diffusion stemming from overheating. These approaches however, do not completely remove overheating, and numerical inaccuracies persist near the interface. In this article, we propose a new version of the GFM called the Efficient Ghost Fluid Method (EGFM) capable of completely eliminating overheating errors, leading to highly accurate solutions near the interface. The EGFM approach has been implemented in IMPACT, a multi-medium, shock physics code, and has been validated against a wide range of 1D and 2D test cases, including problems with surface tension. These include single- as well as multi-medium shock tube problems, various shock-interface interactions, and shock-driven instabilities.

1. Introduction

The Ghost Fluid Method (GFM) was originally proposed by Fedkiw et al. [1] to model contact discontinuities in inviscid, compressible, multi-material flows. The GFM is based on applying physically accurate interfacial boundary conditions at the material interface between different fluids, where such boundary conditions are implemented through the definition of *ghost fluids* in the computational domain. In [2], the authors show that the Rankine–Hugoniot jump conditions, i.e. flux conservation, when applied across the interface, yield interfacial conditions that ensure the continuity of *pressure* and *normal velocity*. In [1], the authors define the ghost fluids based on the interfacial flux conservation discussed above. In a two-fluid system with Fluids A and B, they proposed using the pressure and velocity of Fluid B (Fluid A) for Ghost Fluid A (Ghost Fluid B), while the density of Ghost Fluid A (Ghost Fluid B) is obtained directly from Fluid A (Fluid B) through constant extrapolation.

Often, the GFM is coupled [1–3] with the level set (LS) approach [4], where the LS functions are used to track the location of the interface. This approach results in a *sharp representation* of the interface, which is a central feature of the GFM, when compared with other interface approaches including the VOF method [5], mass fraction methods [6], and gamma-based models [6,7], all of which diffuse the interface over multiple cells, giving rise to 'numerical mixing' between the two fluids. This property of the GFM makes it suitable for simulations of multi-material problems involving interfacial phenomena such as problems with interfacial instabilities, surface tension effects, and evaporation.

Using multi-medium Riemann solvers at the interface to couple fluids governed by different equations of state (EOS) has been shown to result in high-quality numerical solutions at and near the interface, e.g. see [8–10]. To extend this idea to the GFM framework, Liu et al. [11] proposed a modified GFM (MGFM), where approximate Riemann solvers were used to obtain more accurate values for the ghost cells with lower conservation errors (see also [12–14] for a discussion of the applications of the MGFM, and [15] for a description of the accuracy and conservation errors associated with different GFMs). Liu et al. [16] further developed the MGFM idea to simulate compressible fluids coupled to deformable structures in the presence of cavitation in fluids. Furthermore, Hu and Khoo [17] proposed a numerical method called I-GFM, where the ghost values were obtained by real and ghost interactions (see [18] for the application of the I-GFM in the primary breakup of a liquid

* Corresponding author.
E-mail address: Praveen.Ramaprabhu@uncc.edu (P. Ramaprabhu).

https://doi.org/10.1016/j.compfluid.2021.105250
Received 20 June 2021; Received in revised form 19 October 2021; Accepted 25 November 2021
Available online 28 November 2021
0045-7930/© 2021 Elsevier Ltd. All rights reserved.

jet, and [19] for a proposed modification to the I-GFM). Wang et al. [13] proposed a real GFM (RGFM) approach to extend the capabilities of the MGFM, and suggested a novel algorithm for the advection of the LS function. More recently, Xu et al. [20] proposed the practical GFM (PGFM) for compressible multi-medium flows.

Although it leads to a sharp interface, the numerical solution from the GFM can exhibit overheating errors [21], which have been observed in the solutions of Riemann problems and in shock interactions with material interfaces. It has been shown [20] that overheating results from numerical inaccuracies that stem from applying single-medium numerical schemes to the fluid pairs (Fluid A + Ghost Fluid A) and (Fluid B + Ghost Fluid B). Since these schemes are naturally associated with diffusion, they give rise to overheating. In this paper, we first briefly review the approaches to addressing overheating in the GFM in the literature. We then propose a new scheme, the Efficient Ghost Fluid Method (EGFM) to completely eliminate this numerical artifact for both 1D and multi-dimensional flow problems. In 1D EGFM, overheating is removed for any mesh size, while in 2D the errors diminish with increasing mesh resolution.

This paper is organized as follows: In §2, the equations required for modeling compressible multi-medium flows are discussed, while the numerical methods to solve such equations are explained in §3. Section 4 summarizes the previous algorithms for isentropic fixing and discusses the EGFM as a highly accurate method to remove overheating from fluid interfaces, while in §5, the EGFM is applied to shock-interface interaction simulations. In §6, the EGFM is extended to 2D problems. The EGFM is validated in §7 using a wide array of 1D test problems, such as single- and multi-medium shock tubes, various shock-interface interactions, as well as standard 2D simulations, such as problems with radial symmetry, the Richtmyer–Meshkov [22,23] (RM) instability, and shock-air cavity interaction (for more validation problems, see [24]). Finally, some conclusions are drawn in §8.

2. Governing equations

Compressible, inviscid flows are modeled by the Euler equations of gas dynamics, which take the form:

$$\frac{\partial U}{\partial t}+\frac{\partial F(U)}{\partial x}+\frac{\partial G(U)}{\partial y}=0 \tag{1}$$

where U is the vector of conserved variables

$$U=\begin{bmatrix}\rho\\ \rho u\\ \rho v\\ \rho E\end{bmatrix}, \tag{2}$$

while $F(U)$ and $G(U)$ are the flux vectors in the x and y directions, respectively:

$$F(U)=\begin{bmatrix}\rho u\\ \rho u^2+p\\ \rho uv\\ u(\rho E+p)\end{bmatrix},\ G(U)=\begin{bmatrix}\rho v\\ \rho uv\\ \rho v^2+p\\ v(\rho E+p)\end{bmatrix} \tag{3}$$

In the above equations, ρ is the density, u and v are the velocities in the x and y directions, respectively, p is the pressure, and E is the total energy per unit mass defined by $E=e+(u^2+v^2)/2$. The internal energy per unit mass e is related to other thermodynamic variables using the EOS. Here, we use the stiff gas EOS:

$$\rho e=\frac{p+\gamma p_\infty}{\gamma-1} \tag{4}$$

where γ is the ratio of specific heats, and p_∞ is the pressure constant.

For compressible multi-medium flows, the LS equation is also used to track the interface:

$$\frac{\partial \phi}{\partial t}+\vec{V}.\nabla\phi=0, \tag{5}$$

where ϕ is the LS function, and $\vec{V}$ is the velocity vector defined by $\vec{V}=(u,v)$. Note that in general, Eq. (5) must be coupled to Eq. (1) to model multi-medium flows, so that the EOS is also a function of the LS function, i.e. $\gamma=\gamma(\phi)$ and $p_\infty=p_\infty(\phi)$ in Eq. (4). For an example of such a relation, see [7,25]. However, the GFM decouples Eqs. (1) and (5) by appropriately applying the interfacial boundary conditions on each medium through the definition of ghost fluids, and as a result, Eq. (5) can be solved independently.

Moreover, the LS function, which is initialized as a signed distance function, must be reinitialized frequently during the simulation using the equation:

$$\frac{\partial \phi}{\partial \tau}+S(\phi_0)(|\nabla\phi|-1)=0. \tag{6}$$

Eq. (6) is solved iteratively over τ, a fictitious time, while S is the sign function, and ϕ_0 represents the LS function before reinitialization. Solving Eq. (6) to steady state also ensures the normal vectors to the interface ($\widehat{N}=\nabla\phi/|\nabla\phi|$) as well as the interface curvature ($\kappa=\nabla.\widehat{N}$) are computed accurately [2]. In particular, κ is required for surface tension calculations, since the pressure jump imposed by surface tension at the interface is given by $[p]=\sigma\kappa$ [3], where σ is the surface tension of the liquid.

3. Numerical methods

In this section, we describe the numerical methods used in IMPACT; a compressible, multi-medium shock physics code to solve Eqs. (1), (5), and (6). We have used IMPACT to verify the accuracy of the proposed EGFM approach by simulating a wide range of 1D and 2D test problems. To begin, the physical domain is discretized into a rectangular mesh with $\Delta x=\Delta y$ to obtain uniform cells for the finite volume formulation. For Eq. (1), the unsplit version [26] of the Godunov scheme is used as follows:

$$U_{i,j}^{n+1}=U_{i,j}^{n}+\frac{\Delta t}{\Delta x}\left[F_{i-\frac{1}{2}j}-F_{i+\frac{1}{2}j}\right]+\frac{\Delta t}{\Delta y}\left[G_{ij-\frac{1}{2}}-G_{ij+\frac{1}{2}}\right] \tag{7}$$

where for instance $U_{i,j}^{n}$ is the cell average of the vector of conserved variables in Eq. (2) for cell (i,j) at time $t=t^n$, $F_{i-\frac{1}{2}j}$ is the flux vector in Eq. (3) for intercell $\left(i-\frac{1}{2},j\right)$, $G_{ij-\frac{1}{2}}$ is the flux vector in Eq. (3) for intercell $\left(i,j-\frac{1}{2}\right)$, and Δt is the time step size obtained from the CFL condition. Numerical fluxes $F_{i\mp\frac{1}{2}j}$ and $G_{ij\mp\frac{1}{2}}$ are computed by defining 1D Riemann problems at the intercells $\left(i\mp\frac{1}{2},j\right)$ and $\left(i,j\mp\frac{1}{2}\right)$ in the x and y directions, respectively. In this work, the fluxes are calculated using the Roe Riemann solver [27]. In order to achieve high-order accuracy in solving Eq. (7), the fifth-order WENO reconstruction [28,29] is also applied to cell averages $U_{i,j}^{n}$ in a direction-by-direction fashion [30] before the Roe solver is applied.

Note that Eq. (7) is solved for each medium separately. Thus, after Ghost Fluid A and Ghost Fluid B have been defined, Eq. (7) is applied to the fluid pairs (Fluid A + Ghost Fluid A) and (Fluid B + Ghost Fluid B) independently to obtain the solution at the next time-step. In the next section, the EGFM is introduced to apply the interfacial boundary conditions accurately to resolve multi-medium shock tubes and shock-interface interactions.

To solve Eq. (5), we use the extended interface velocity to advect the LS function. To obtain such a velocity field, the interface velocity is first

obtained by solving multi-medium Riemann problems (MMRPs) in the normal direction to the interface ($\widehat{N}$). The interface velocity is then extrapolated to both sides of the interface using the constant extrapolation equation

$$\frac{\partial I}{\partial \tau} + \widehat{N}.\nabla I = 0, \tag{8}$$

which is solved over fictitious time τ to steady state. In Eq. (8), I can represent the normal velocity V_N or any other variable to be extrapolated. Once the extended velocity field has been obtained, Eq. (5) is solved by first writing

$$\frac{\partial \phi}{\partial t} + \frac{V_N \phi_x}{\sqrt{{\phi_x}^2 + {\phi_y}^2}}\phi_x + \frac{V_N \phi_y}{\sqrt{{\phi_x}^2 + {\phi_y}^2}}\phi_y = 0, \tag{9}$$

and then using the Godunov scheme as proposed by Osher and Fedkiw [2]. Note that Eq. (9) is solved in a band of cells using the Fast Local LS Method of Peng et al. [31] in which the extended velocity field is modified as $c(\phi)V_N$, where $c(\phi)$ is the correction coefficient. For 1D problems in this paper, however, the extended velocity using the approach of Wang et al. [13] is employed, which guarantees the signed distance function is maintained, so that the reinitialization is no longer required. For 2D problems, the LS function is reinitialized by solving Eq. (6) to steady-state using the methods in [32], which yield second-order accuracy and ensure the interface does not move during the reinitialization. Finally, time discretization in IMPACT is handled using a third-order TVD-RK method [33], where Eqs. (7) and (9) are solved simultaneously from time-step n to $n+1$, and then ϕ^{n+1} is reinitialized using Eq. (6) (see [1] for details).

4. Methods to address overheating and the Efficient Ghost Fluid Method

To address overheating, Fedkiw et al. [1] proposed extrapolating the entropy rather than the density, since the entropy field is less susceptible to overheating errors [21]. In addition, the authors suggested an isentropic fix, where for an interface located between cells 'i' and '$i+1$,' the entropy of cell '$i-1$' is used to "fix" the entropy of cell 'i' and to populate the ghost cells (see [1] for details).

Overheating can be viewed as stemming from excessive entropy generation [1,21], from spurious sources at or near the interface. A successful treatment for overheating should accommodate entropy generation in the computational domain to correctly capture the waves and converge to the weak solution, while removing overheating from the interface. As we will see in the rest of this section and in §7, the EGFM not only leads to the proper solution for rarefactions and shock waves in the domain, but also eliminates overheating and yields highly accurate solutions near the interface free of excessive and spurious entropy generation

In versions of the GFM [11,13,20] which rely on the solution to MMRPs at the interface, it has been shown that using the cell values from '$i-1$' and '$i+2$' as initial conditions for the MMRP resulted in an improvement in reducing overheating (when compared with the choice of using data from 'i' and '$i+1$'). In the MGFM [11] approach, the entropy values of the real cells next to the interface were fixed by the solution to the MMRP, which showed further improvement in reducing the overheating error. In the RGFM [13] approach, real cells next to the interface were corrected for density, velocity, and pressure values, rather than for entropy, as seen in Fig. 1 (based on Fig. 4 from Xu and Liu [15]). This resulted in more accurate imposition of boundary conditions at the interface, and in an improved behavior in shock impedance matching problems [11] by reducing the amplitude of the erroneous numerical wavelets reflecting off the interface.

As an alternative to the approach outlined in [1], the isentropic fix can also be implemented using more sophisticated methods such as

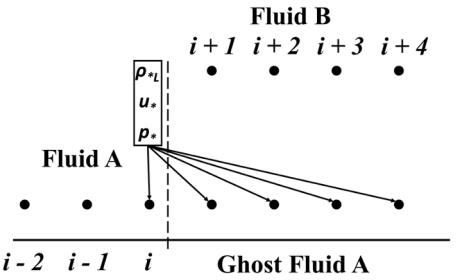

Fig. 1. The isentropic fix and population of the ghost cells in the RGFM. Figure is modified from Fig. 4 in [15].

those outlined in the PGFM [20] approach where the isentropic relation is applied between a reference cell (with density ρ_r and pressure p_r) located far from the interface and the cell next to the interface. By comparing the pressures, either isentropic or shock relations are used for the density [20]

$$\rho_k = \begin{cases} \rho_r \left(\dfrac{p_k + p_{\infty A}}{p_r + p_{\infty A}}\right)^{\frac{1}{\gamma_A}}, & p_k \le p_r \ (rarefaction) \\ \rho_r \left[\dfrac{(\gamma_A - 1)(p_r + p_{\infty A}) + (\gamma_A + 1)(p_k + p_{\infty A})}{(\gamma_A - 1)(p_k + p_{\infty A}) + (\gamma_A + 1)(p_r + p_{\infty A})}\right], & p_k > p_r \ (shock) \end{cases} \tag{10}$$

where k denotes the points where the density fix is to be applied (see [20] for details).

Unfortunately, the above methods, while reducing overheating errors, do not completely eliminate them. Since overheating stems from numerical inaccuracies associated with single-medium solvers, coupling an isentropic fix with such solvers will still result in diffusion (albeit to a smaller extent) near the interface. We show the efficient approach to eliminating overheating is that the isentropic fix (or any similar numerical remedy) must be applied *after* the solution from the single-medium solver has been obtained. This idea is similar to Cocchi and Saurel [10], where in the front-tracking context, the numerical solution is corrected using a predictor-corrector step and interpolations between the values of the cells next to the interface. We now describe an alternative approach, the EGFM, to completely remove overheating from fluid interfaces.

4.1. The EGFM approach

First, we recall that in the GFM framework, compressible multi-medium flows are treated by splitting *the two-fluid Riemann problem* $RP(U_L, U_R)$ *into two single-fluid Riemann problems* $RP(U_L, U_{*L})$ *and* $RP(U_{*R}, U_R)$ (see [15] for details), where U_{*L} and U_{*R} are obtained from the solution to the two-fluid Riemann problem $RP(U_L, U_R)$. Considering $RP(U_L, U_R)$ in Fig. 2(a), note that in the immediate aftermath of the removal of the 'diaphragm' between Fluids A and B, two new values (U_{*L} and U_{*R}) emerge in the solution, on the left and right sides of the interface, respectively. The fluids then interact with these new values, i.e. in Fluid A, U_L and U_{*L} form a leftward rarefaction wave, and in Fluid B, U_{*R} and U_R form a rightward shock wave. The jump between Fluids A and B, however, moves by the linearly degenerate field which is the interface velocity. The above process occurs in the same manner in Fig. 2 (b)–(c); U_{*L} in Fig. 2(b) interacts with U_L to form a rarefaction wave, while U_{*R} in Fig. 2(c) interacts with U_R to form a shock wave. Fig. 2 demonstrates both the initial condition and the global solution at $t = t_1$. Also note that in Fig. 2(b)–(c), the solutions in the real parts of the domains are of interest, since they determine the eventual solution to the original problem in Fig. 2(a) (see [20] for various possible solutions in the ghost regions).

Based on the previous discussion, we now describe the EGFM approach to address overheating errors. In Fig. 3(a), the Riemann problem $RP(U_L, U_{*L})$ is solved numerically over one time-step Δt using a

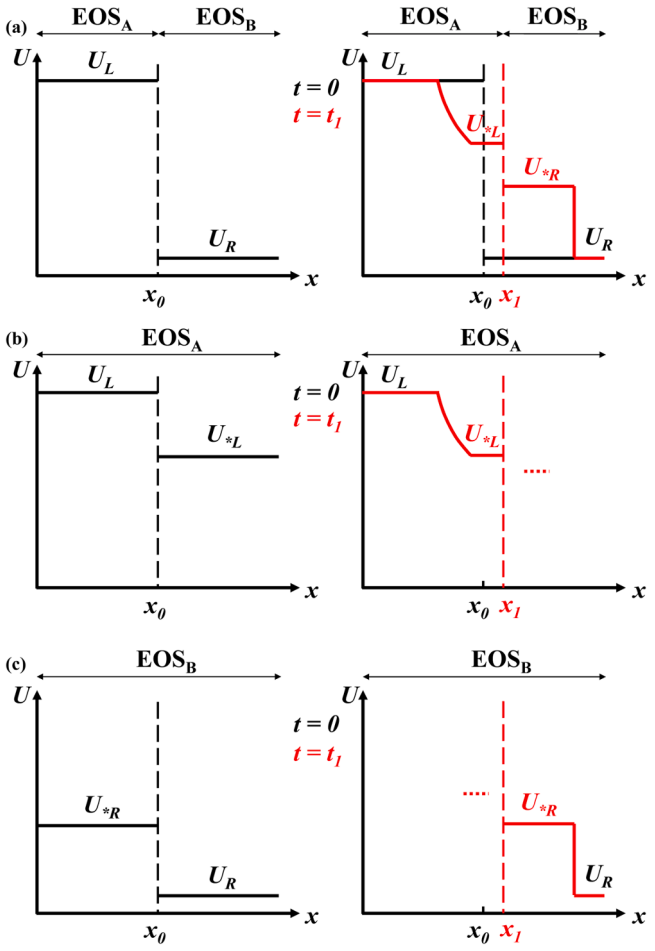

Fig. 2. (a) Two-fluid Riemann problem $RP(U_L, U_R)$ with EOS_A and EOS_B. (b) Single-fluid Riemann problem $RP(U_L, U_{*L})$ for Fluid A (EOS_A). (c) Single-fluid Riemann problem $RP(U_{*R}, U_R)$ for Fluid B (EOS_B). The initial condition is shown in black, while the solution at $t = t_1$ is shown in red. The initial location of the interface is $x = x_0$ (black dashed line), while the interface location at $t = t_1$ is $x = x_1$ (red dashed line).

single-medium solver with EOS_A. Note that this changes the value of some cells near the initial interface marked by red symbols, which indicate the solution affected by numerical diffusion from applying the single-medium solver. We then apply the following corrections at cell 'k' in two steps (we have indicated the values obtained from the single-medium solver (red) and the corrected values (green) using the subscripts 's' and 'c' respectively).

Step (1): The value of the cell next to the new interface (at $t = \Delta t$) is changed to U_{*L}, which is the exact solution immediately following the removal of the diaphragm:

$$-\Delta x < \phi_k^{(\Delta t)} \leq 0 \rightarrow U_c = U_{*L}, \tag{11}$$

where $\phi_k^{(\Delta t)}$ is the LS function at cell 'k' at $t = \Delta t$.

Step (2): Similar to the PGFM [20] approach, in the case of a left rarefaction the isentropic relation is then applied between the cell next to the new interface and the cells away from it (within a computational stencil) to obtain the corrected values. Note that in this second step, the isentropic relation is applied not only to densities (as in [20]), but also to cell velocities, as follows:

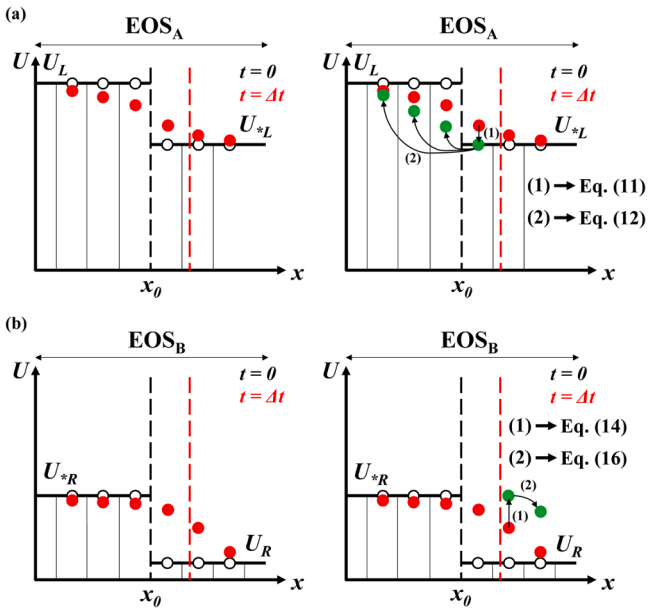

Fig. 3. The EGFM-V1 implementation for (a) Fluid A and (b) Fluid B. The initial location of the interface is depicted by the black dashed line ($x = x_0$), and the interface location at $t = \Delta t$ is demonstrated by the red dashed line. The initial condition is shown in black, while the solution at $t = \Delta t$ is shown in red. The numerical corrections are carried out in two steps labeled by (1) and (2), and the corrected values are shown in green. (For interpretation of the references to color in this figure legend, the reader is referred to the web version of this article.)

$$-n\Delta x < \phi_k^{(\Delta t)} \leq -\Delta x \rightarrow \begin{cases} \rho_c = \rho_{*L}\left(\dfrac{p_s + p_{\infty A}}{p_{*L} + p_{\infty A}}\right)^{\frac{1}{\gamma_A}}, \\ u_c = u_* + \dfrac{2}{\gamma_A - 1}(a_{*L} - a_s), \end{cases} \tag{12}$$

where $a_s = \sqrt{\gamma_A(p_s + p_{\infty A})/\rho_s}$ is the speed of sound, and n is the number of cells to be corrected, which can be chosen to coincide with the computational stencil used for the LS calculation. Similarly, for a left shock, the following relations are applied in step (2):

$$-n\Delta x < \phi_k^{(\Delta t)} \leq -\Delta x \rightarrow \begin{cases} \rho_c = \rho_{*L}\left[\dfrac{(\gamma_A - 1)(p_{*L} + p_{\infty A}) + (\gamma_A + 1)(p_s + p_{\infty A})}{(\gamma_A - 1)(p_s + p_{\infty A}) + (\gamma_A + 1)(p_{*L} + p_{\infty A})}\right], \\ u_c = u_* - a_s\left(\dfrac{\rho_s}{\rho_{*L}} - 1\right)\sqrt{\dfrac{\gamma_A + 1}{2\gamma_A}\dfrac{p_{*L} + p_{\infty A}}{p_s + p_{\infty A}} + \dfrac{\gamma_A - 1}{2\gamma_A}}, \end{cases} \tag{13}$$

We found that applying just the density fix in Eqs. (12),(13) (as suggested in [20]) was insufficient in addressing overheating, without the accompanying velocity fix. The above steps are depicted with the labels (1) and (2) in Fig. 3(a). The corresponding fix applied to Fluid B is shown in Fig. 3(b), where the Riemann problem $RP(U_{*R}, U_R)$ is solved numerically for one timestep with EOS_B. Once again, the red symbols are associated with numerical inaccuracies, and the correction (shown in Fig. 3(b) as red → green) is applied in two steps, which mirror Eqs. (11)–(13) for Fluid B. The complete set of equations for Fluids A and B are summarized in Table 1.

In 1D, the wave types that determine the specific corrections to be applied are identified using pressure as the criterion. Thus, for Fluid A if $p_s \geq p_{*L}$, then Eq. (12) is used to apply the correction, otherwise Eq. (13) is employed. Similarly, for Fluid B if $p_{*R} \leq p_s$, then Eq. (15) is applied, while Eq. (16) is used for a right shock. Note that in 1D, pressure is sufficient as a criterion to determine the wave types, but in 2D the presence of curvature effects will lead to pressure variations, requiring a

Table 1
Summary of corrections applied to the cell values for Fluids A and B in the EGFM algorithm.

Fluid A			$U_c = U_{*L}$ (11)
	Step 1: $-\Delta x < \phi_k^{(\Delta t)} \leq 0$	left rarefaction ($p_s \geq p_{*L}$)	$\rho_c = \rho_{*L}\left(\frac{p_s + p_{\infty A}}{p_{*L} + p_{\infty A}}\right)^{\frac{1}{\gamma_A}}$ (12)
	Step 2: $-n\Delta x < \phi_k^{(\Delta t)} \leq -\Delta x$	left shock ($p_s < p_{*L}$)	$u_c = u_* + \frac{2}{\gamma_A - 1}(a_{*L} - a_s)$ $\rho_c = \rho_{*L}\left[\frac{(\gamma_A - 1)(p_{*L} + p_{\infty A}) + (\gamma_A + 1)(p_s + p_{\infty A})}{(\gamma_A - 1)(p_s + p_{\infty A}) + (\gamma_A + 1)(p_{*L} + p_{\infty A})}\right]$ (13)
Fluid B	Step 1: $0 < \phi_k^{(\Delta t)} \leq \Delta x$	right rarefaction ($p_{*R} \leq p_s$)	$u_c = u_s - a_s\left(\frac{\rho_s}{\rho_{*L}} - 1\right)\sqrt{\frac{\gamma_A + 1}{2\gamma_A}\frac{p_{*L} + p_{\infty A}}{p_s + p_{\infty A}} + \frac{\gamma_A - 1}{2\gamma_A}}$ $U_c = U_{*R}$ (14)
	Step 2: $\Delta x < \phi_k^{(\Delta t)} \leq n\Delta x$		$\rho_c = \rho_{*R}\left(\frac{p_s + p_{\infty B}}{p_{*R} + p_{\infty B}}\right)^{\frac{1}{\gamma_B}}$, (15)
		right shock ($p_{*R} > p_s$)	$u_c = u_* + \frac{2}{\gamma_B - 1}(a_s - a_{*R})$,
			$\rho_c = \rho_{*R}\left[\frac{(\gamma_B - 1)(p_{*R} + p_{\infty B}) + (\gamma_B + 1)(p_s + p_{\infty B})}{(\gamma_B - 1)(p_s + p_{\infty B}) + (\gamma_B + 1)(p_{*R} + p_{\infty B})}\right]$ (16)
			$u_c = u_* + a_s\left(\frac{\rho_s}{\rho_{*R}} - 1\right)\sqrt{\frac{\gamma_B + 1}{2\gamma_B}\frac{(p_{*R} + p_{\infty B})}{(p_s + p_{\infty B})} + \frac{\gamma_B - 1}{2\gamma_B}}$

modified approach. In §6, we propose using the Riemann invariant $(p + p_\infty)/\rho^\gamma$ as a criterion for wave identification in multidimensions, since it is compatible with both liquids and gases.

The modifications to the numerical solution using the analytical relations discussed above form the basis of the EGFM approach. We term this algorithm EGFM Version 1 (EGFM-V1) in the rest of this article. In Eqs. (12), (13), (15), and (16), we have used p_{*L} and p_{*R} for the interfacial pressures, to allow for the general case when surface tension is present. In the absence of surface tension, we use $p_* = p_{*L} = p_{*R}$.

In the EGFM approach described above, the MMRP between Fluids A and B needs to be solved only once. In other words, assuming the interface is initially located between cells i and $i+1$, the MMRP $RP(U_i, U_{i+1})$ is solved to obtain U_{*L} and U_{*R} (ρ_{*L}, ρ_{*R}, u_*, p_{*L}, p_{*R}), while the exact multi-medium Riemann solver subroutine or function is not called for the rest of the simulation. As a result, we use the label 'Efficient' for this version of the GFM. Based on the computed values of U_{*L} and U_{*R}, the numerical corrections discussed are applied to advance the solution over one sub-step of a multi-step time integration method using the following EGFM-V1 algorithm:

(i) Use U_{*L} to define Ghost Fluid A at cells $i+1$, $i+2$, $i+3$, etc.
(ii) Use U_{*R} to define Ghost Fluid B at cells i, $i-1$, $i-2$, etc.
(iii) Apply an appropriate reconstruction, e.g. WENO to (Fluid A + Ghost Fluid A) and (Fluid B + Ghost Fluid B) separately.
(iv) Find fluxes and advance the solution for (Fluid A + Ghost Fluid A) and (Fluid B + Ghost Fluid B) separately over a sub-step of a multi-step time integration method such as TVD-RK.
(v) Using u_*, advance the LS function over the same sub-step.
(vi) Fix the value of the cell next to the new interface and located in Fluid A to U_{*L}, and the value of the cell next to the new interface and located in Fluid B to U_{*R}.
(vii) Apply either the isentropic or the shock relation between the cells next to the new interface, and the cells further from it to fix densities and velocities.
(viii) Form the actual solution domain based on the fixed solutions to Fluid A and Fluid B.

Note that the novelty of our approach lies in steps (vi) and (vii). A few observations are in order:

1 While step (1) of the fix in Fig. 3 is implemented for only a single point, step (2) may be applied to one or more points. We recommend using the same stencil width, used for the computation of the LS method on each side of the interface (5 points in our simulations [31]).
2 Fig. 3 shows the numerical fixes applied in conjunction with a simple forward Euler method for time discretization. For multi-step approaches such as the TVD-RK method, the corrections must be implemented over each sub-step, i.e. the LS function is first advanced over the sub-step, followed by application of the corrections using the above protocol.
3 The EGFM can be coupled with approximate Riemann solvers (ARS), for materials with uncertainties in the EOS that do not permit an exact solution to the Riemann problem. Consider the approximate solution to $RP(U_L, U_R)$ obtained from an ARS and given by (U_{aL}, U_{aR}). Since U_{aL} and U_{aR} are different from U_{*L} and U_{*R}, an overheating error is introduced in step (1) of the fix in Fig. 3, the magnitude of which will depend on the accuracy of the approximate solver. In §7, we evaluate the extent of overheating errors when the EGFM is coupled to a linearized Riemann Solver (LRS), and find that while overheating errors are not eliminated, they are still significantly reduced.
4 If the Riemann problem shown in Fig. 2 involves a shock wave, i.e. $\text{EOS}_\text{A} = \text{EOS}_\text{B}$ and U_L and U_R are the post- and pre-shock values of the shock, respectively, the above method cannot remove the numerical inaccuracies and will result in a diffuse shock. Consequently, the

above implementation must be modified to be compatible with problems involving shock waves (including single shock and shock-interface interactions). This is described in the next section.

5 In Fig. 3, assigning U_{*L} and U_{*R} in step (1) to the cells next to the new interface may lead to slight displacements of the left and right waves from their actual positions. To avoid this, we propose the EGFM Version 2 (EGFM-V2), where step (1) in Fig. 3 is skipped, and the isentropic and shock relations are applied directly between the interfacial values (U_{*L} and U_{*R}) and the cells on the left ($-n\Delta x < \phi_k^{(\Delta t)} \leq 0$) and right ($0 < \phi_k^{(\Delta t)} \leq n\Delta x$) sides of the new interface.

Note that approaches such as the RGFM [13] algorithm or the proposed GFM algorithm in [34] correct the real cell values next to the interface for density, velocity, and pressure, as shown in Fig. 1. However, this can slightly displace the rarefaction and shock waves in the numerical solution, even though the real cell correction is implemented before applying the single-medium solvers (we will also see in 2D results that such a correction can lead to unphysical wiggles and spurious oscillations at the interface). The EGFM-V1 can suffer from the same displacement error, with the difference that the real cells are corrected in step (1) after the solution from single-medium solvers has been obtained. The EGFM-V2, however, corrects this drawback and leads to the formation of rarefaction and shock waves at their correct positions. In §7, the EGFM-V1, EGFM-V2, RGFM, and the original GFM [1] (OGFM) are compared to highlight this wave placement issue.

5. Application of the Efficient Ghost Fluid Method to shock-interface interactions

A framework for applying the EGFM to shock-interface interactions in 1D is presented in this section (note that a similar implementation in multi-dimensions will require the definition and tracking of a second level set field, which is beyond the scope of this article and therefore was not included in the current work). Consider the problem configuration in Fig. 4, in which a shock is located at x_{S0} and a material interface is at x_0. To implement the EGFM for shock-interface problems, care must be taken to ensure the incident shock remains sharp as it impinges on the interface. Initially sharp shock fronts that have diffused numerically in time are not compatible with the EGFM approach, since such shock waves already contain numerical errors. In the following, we discuss an implementation of the EGFM in which the shock is maintained as a sharp front.

In Fig. 4, the initial boundary between U_S and U_L, i.e. post- and pre-shock states, moves to the right with shock speed given by the Rankine–Hugoniot jump conditions:

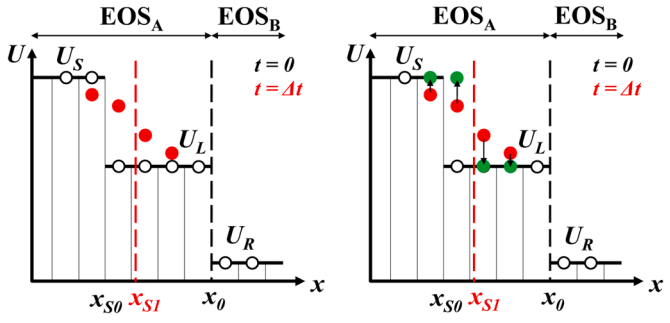

Fig. 4. Shock-interface interaction problem with the fix described in §5. The initial locations of the shock and the interface are $x = x_{S0}$ and $x = x_0$, respectively. The shock location at $t = \Delta t$ is $x = x_{S1}$ (red dashed line). The initial condition is shown in black, while the solution at $t = \Delta t$ is shown in red. The numerical corrections are applied to the cells around $x = x_{S1}$, and the corrected values are shown in green. (For interpretation of the references to color in this figure legend, the reader is referred to the web version of this article.)

$$S = \frac{\rho_S u_S - \rho_L u_L}{\rho_S - \rho_L} \tag{17}$$

The diffuse shock is fixed by first computing the location of the shock according to $x_{S1} = x_{S0} + S\Delta t$, where Δt is obtained from the CFL condition. If a cell center is located behind (in front of) x_{S1}, its value is changed to the post-shock U_S (pre-shock U_L) value. Our numerical simulations show that fixing only two cells on either side of the shock is sufficient to completely remove diffusion. The explained fix holds for shocks traveling in the negative x-direction as well. As before, for a multi-step time integration method such as TVD-RK, the shock location x_S is first found in each sub-step using multi-step equations, and the shock fix is then applied using the above approach.

We thus propose computing sharp shock-interface interactions using the following approach; if $x_{S1} < x_0 - 0.5\Delta x$, the above shock treatment must be applied. However, if $x_0 - 0.5\Delta x \leq x_{S1}$ (the shock has reached the interface), only the two cells behind the shock are fixed, followed by applying the EGFM (either V1 or V2) for the rest of the simulation. Note that for this condition, the EGFM handles $RP(U_S, U_R)$. For shock-interface interactions with a leftward shock impacting the interface from the right, the procedure is changed by comparing x_{S1} with $x_0 + 0.5\Delta x$, while the EGFM solves $RP(U_L, U_S)$.

6. Extension of the Efficient Ghost Fluid Method to 2D problems

In this section, we present an extension of the EGFM to 2D problems. For these problems, exact solutions to the MMRPs are not available, and a widely used [11,13,15,20,34] technique to circumvent this issue is to construct 1D MMRPs in the normal direction to the interface using local density, *normal* velocity (V_N), and pressure on the "*left*" and "*right*" sides of the interface. In other words, at the scale of the cell dimensions ($\sim \Delta x$), the interface is treated as having negligible curvature. Such an approximation is justified when an adequate mesh resolution is employed, and/or when the interface is devoid of highly curved regions ($\kappa\Delta x \ll 1$).

We use the same approach to extend the EGFM to 2D, but note that unlike the 1D case, such an extension is approximate at cells further away from the interface, and may allow some overheating to persist, ultimately vanishing for $\kappa\Delta x \ll 1$. The specific approach of Sambasivan and Udaykumar [34] (hereafter referred as RGFM2 in this paper) is used and modified here. In this approach, 1D MMRPs are constructed using normal vectors and bilinear interpolations, as shown by Fig. 5 (based on Fig. 1 from [35]). In this figure, point P is located next to the interface, $\widehat{N}$

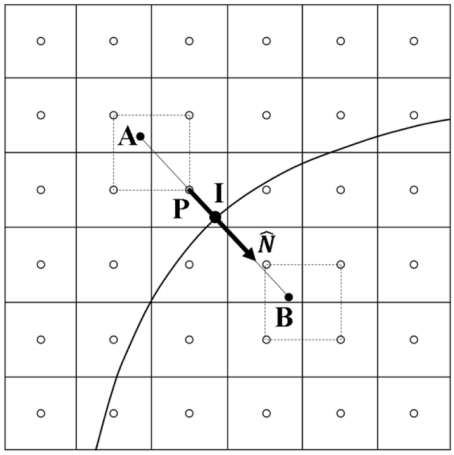

Fig. 5. Construction of an MMRP at the interface using the normal vector and bilinear interpolation. Point P is located next to the interface, point I is on the interface, while points A and B are $1.5\Delta x$ away from the interface. Figure is modified from Fig. 1 in [35].

is the normal vector at P, point I is on the interface ($\phi = 0$), and points A and B are located in Fluids A and B, respectively, each at a normal distance of $1.5\Delta x$ from the interface. The procedure to find the locations of these points, and to form the 1D MMRP between points A and B are described in [34]. Note that we take Fluid A (Fluid B) to be the "*left*" ("*right*") fluid where $\phi \leq 0$ ($\phi > 0$).

In [34], the authors apply the correction to the real fluid using the RGFM [13] approach by replacing the values at point P by the solution to the 1D MMRP in the interface normal direction. However, we observe in our simulations that in 2D, such a correction can lead to unphysical wiggles and spurious oscillations at the interface. Moreover, as mentioned in the last observation in §4, this can misplace the waves in the domain. Once such a correction has been applied to all the real cells next to the interface, a one-sided extrapolation is implemented to populate the ghost values [13,34]. We use the same extrapolation method here to populate the ghost cells, but in contrast to RGFM [13] and RGFM2 [34], the real cell correction is not applied, since the EGFM does not fix the real fluid until *after* the numerical solution from single-medium solvers has been obtained. The procedure to implement the EGFM in 2D is shown in Fig. 6.

In Fig. 6, the interface between Fluids A and B at $t = 0$ has been labeled $\phi^{(0)} = 0$. For the EGFM implementation, U_{*L} and U_{*R} must be available to the cells whose values are to be corrected. Similar to the 1D situation, these cells are located next to the new interface at $t = \Delta t$ (labeled $\phi^{(\Delta t)} = 0$) in Fig. 6. Since the direction of interface movement is not known *a priori*, U_{*L} and U_{*R} must be made available to cells on both sides of the interface. In practice, this is achieved by extrapolating in the direction opposite to that used for obtaining the ghost fluids. If a multi-step time integration method such as TVD-RK is used, the new location of the interface is first determined for each sub-step, before the corrections can be applied.

Eqs. (11)–(16) apply 1D relations to 2D problems without consideration of the effect of the interface curvature, and can lead to errors at cells located further away from the interface. To mitigate this issue, we implement the EGFM only at the cells next to the new interface, i.e. for EGFM-V1, step (2) is skipped; while for EGFM-V2, the isentropic and shock relations are applied to cells satisfying $|\phi_{ij}^{(\Delta t)}| \leq \Delta x$. If the EGFM is to be applied to cells located further away from the interface, the 1D MMRPs must take into account the interface curvature effects by including the following geometric source terms

$$S = \kappa \begin{bmatrix} \rho V_N \\ \rho V_N^2 + p \\ V_N(\rho E + p) \end{bmatrix}, \tag{18}$$

where κ is the interface local curvature defined as $\nabla.\widehat{N}$ (see [26] for similar source terms used in 1D representation of 2D problems with radial symmetry). Combining Eq. (18) with the 1D MMRP results in modified isentropic and shock relations that accurately capture the interface curvature effects in the entire domain, and will lead to a more accurate implementation of the EGFM in multi-dimensions. However, since we are primarily concerned with applications where the near-interface flow field is of the most significance (such as flows with surface tension), this treatment is deferred to a later publication, while noting the errors that stem from this approximation vanish for $\kappa\Delta x \ll 1$.

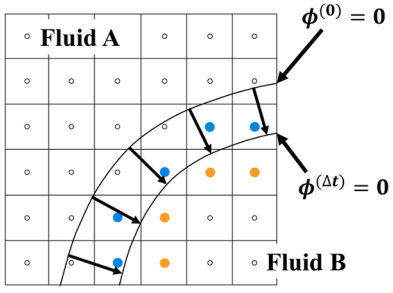

Fig. 6. The EGFM implementation in 2D; the interface has been labeled $\phi^{(0)} = 0$ and $\phi^{(\Delta t)} = 0$ at $t = 0$ and $t = \Delta t$, respectively. The cell values next to the new interface ($\phi^{(\Delta t)} = 0$) are corrected to address overheating.

Finally, we propose the following criterion to distinguish between isentropic or shock relations in multi-dimensions. In contrast to the 1D situation, the pressure field in 2D flows cannot be used for this purpose, since it can vary behind the shock wave depending on the shock curvature (or the pressure behind a rarefaction wave may increase after its formation). In this article, we suggest using the Riemann invariant $(p + p_\infty)/\rho^\gamma$ as a criterion, since it is compatible with both liquids and gases in Eq. (4). Note that $(p + p_\infty)/\rho^\gamma$ remains unchanged in a rarefaction or smooth regions of the flow, while increasing after the passage of a shock wave. Note that for gases $p_\infty = 0$, and the equation for entropy constancy in the smooth regions of the flow is recovered. Therefore, for the cells in Fluid A in Fig. 6, if $(p_{ij}^{(\Delta t)} + p_{\infty A})/[\rho_{ij}^{(\Delta t)}]^{\gamma_A} \geq (p_{*L} + p_{\infty A})/\rho_{*L}^{\gamma_A}$, then Eq. (12) is applied to fix $\rho_{ij}^{(\Delta t)}$ and $V_{Nij}^{(\Delta t)}$, while $V_{Tij}^{(\Delta t)}$ remains unchanged. Otherwise, Eq. (13) is used. Similarly, for the cells in Fluid B, if $(p_{*R} + p_{\infty B})/\rho_{*R}^{\gamma_B} \leq (p_{ij}^{(\Delta t)} + p_{\infty B})/[\rho_{ij}^{(\Delta t)}]^{\gamma_B}$, then Eq. (15) is employed, otherwise Eq. (16) is applied. As before, for a multi-step time integration method such as TVD-RK, the new location of the interface is first found for each sub-step, before the corrections can be applied.

7. Results and discussion

7.1. 1D test problems

In this section, we report numerical solutions from different 1D problems using the OGFM, RGFM, EGFM-V1, and EGFM-V2 algorithms, and analyze the results to evaluate the performance of the EGFM in comparison to the other methods. Results from the *shock impedance matching* problem are presented first, since it has been widely used in assessing the performance of variations of the GFM, including the MGFM [11], RGFM [13], and PGFM [20].

The numerical results from IMPACT are compared with exact solutions for density, velocity, pressure, entropy, and temperature (or internal energy) for each case. For all the test cases reported in this section, a domain size of unity was used. To evaluate the performance of the EGFM in capturing the waves, we report the L_1 norm of error in density computed for rarefaction waves as $L_1 = \sum_{i=1}^{N} |\rho(x_i) - \rho_i|/N$, where $\rho(x_i)$ and ρ_i are the exact and numerical densities at cell 'i'. We calculate the L_1 norm on $[x_a, x_b]$, where x_a and x_b are located on the left and right sides of a rarefaction wave respectively, and report the order of convergence for each scheme.

7.1.1. Shock impedance matching problem [11,13, 20]

In this multi-medium shock tube problem, the solution comprises a shockwave to the right of the original discontinuity, while no wave is present to the left. Validation efforts of previous GFM algorithms [11,13, 20] have plotted dimensionless density, velocity, and pressure to evaluate the numerical results. In addition to these quantities, we also plot entropy defined as $s = s_0 + \ln(p/\rho^\gamma)$ [26] where the constant s_0 is arbitrarily chosen to be unity. The domain is filled with two different gases ($\gamma_L = 1.667$ and $\gamma_R = 1.2$) with a discontinuity at $x_0 = 0.2$, and the following initial condition

$$W_L = (\rho_L, u_L, p_L) = (3.174819866, 9.434397965, 100),$$

$$W_R = (\rho_R, u_R, p_R) = (1, 0, 1).$$

The solution obtained at $t = 0.06$ for a mesh of 80 cells and $CFL = 0.3$ [30] is shown in Fig. 7.

As seen in Fig. 7, the EGFM completely eliminates the unphysical

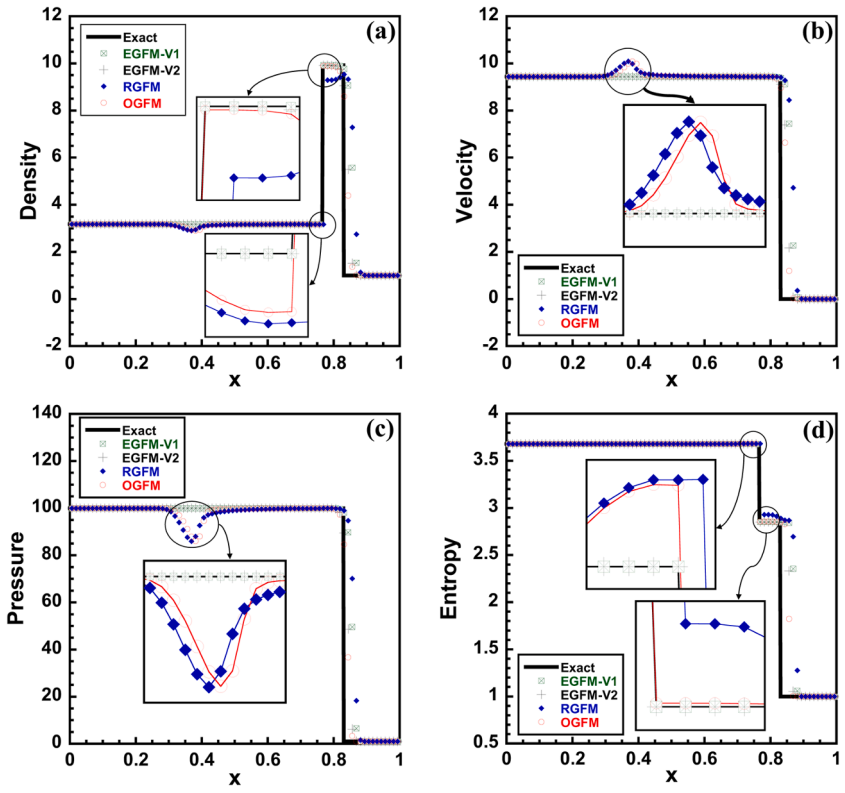

Fig. 7. The numerical solutions from the OGFM, RGFM, EGFM-V1, and EGFM-V2 compared to the exact solution for (a) density, (b) velocity, (c) pressure, and (d) entropy for problem 7.1.1. The plots indicate the EGFM removes overheating and the spurious numerical reflections, while the OGFM and RGFM exhibit errors.

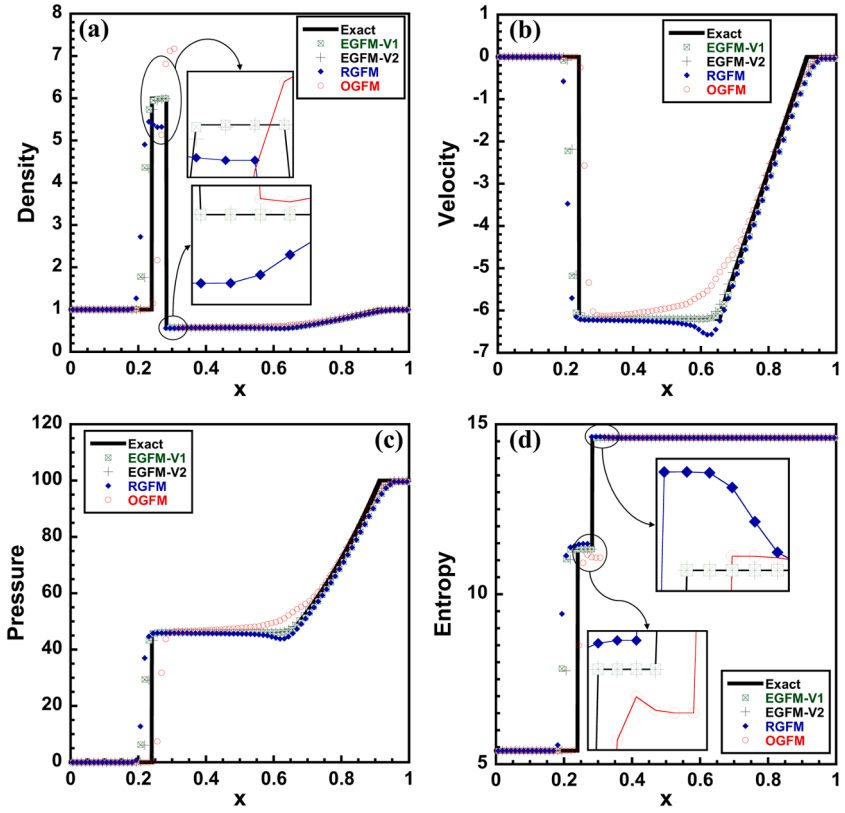

Fig. 8. The numerical solutions of Problem 7.1.2 by the OGFM, RGFM, EGFM-V1, and EGFM-V2 compared to the exact solution for (a) density, (b) velocity, (c) pressure, and (d) entropy. Both EGFM versions remove overheating and the erroneous feature on the rarefaction corner.

reflecting wave to the left of the interface. Note that the OGFM and RGFM solutions contain numerical errors and spurious reflections, since they apply approximate boundary conditions at the interface. The EGFM solution however, exactly matches the analytical values, since it applies the exact interfacial boundary conditions. In earlier efforts to simulate this problem, including the MGFM [11], RGFM [13], and PGFM [20] approaches, the erroneous reflections observed in Fig. 7 were not completely removed, but mitigated in some instances.

The insets in Fig. 7 also show the solution detail across the interface for the density and entropy profiles, and demonstrate the results from the EGFM are in excellent agreement with the analytical solution, while the OGFM and RGFM exhibit some overheating. In Fig. 7(a) and (d), the interface location computed using the RGFM is displaced one mesh cell away from the exact location. Note that although the RGFM (as well as the MGFM [11], PGFM [20], and RGFM2 [34]) is based on obtaining multi-medium Riemann solutions at the interface, the MMRP defined at the interface is based on the cell values that could already be contaminated with overheating. The EGFM, however, fixes the cell values next to the interface, and applies the correct interfacial boundary conditions for each time step/sub-step. These issues are exacerbated for problems containing strong shocks (high pressure ratios), and are illustrated in the subsequent problems.

7.1.2. Shock tube with strong pressure jump [26]

In this non-dimensional shock tube problem, the initial condition contains a strong pressure jump with a pressure ratio 10,000:1. The computational domain is filled with air ($\gamma = 1.4$) with the initial discontinuity located at the center ($x_0 = 0.5$). The complete initial condition data is given by

$$W_L = (\rho_L, u_L, p_L) = (1, 0, 0.01),$$

$$W_R = (\rho_R, u_R, p_R) = (1, 0, 100).$$

The solution thus consists of a left shock and a right rarefaction, and is shown for $t = 0.035$ in Fig. 8 where a mesh of 80 cells with $CFL = 0.3$ was utilized in the simulations. In this figure, the OGFM and RGFM exhibit some errors near the rarefaction corner (see [11] and [15] where similar behavior has been reported for these versions of the GFM). For the contact discontinuity, these approaches give rise to overshoots and undershoots and miscalculate the location of the wave by a couple of cells. As discussed in Problem 7.1.1, this behavior results from the approximations in capturing the interfacial boundary conditions. In the OGFM implementation, as pointed out in [1], the conservation of mass, momentum, and energy is relaxed at the contact discontinuity, which can give rise to inaccurate prediction of the location of the wave. This leads to incorrect values for the interface location (see [11] for example), particularly for problems with strong shocks. In contrast, when the EGFM approach is applied, highly accurate numerical solutions are obtained, overheating and the erroneous feature on the rarefaction corner are completely eliminated, and the contact wave location is properly calculated.

For computing the error in density, we choose $x_a = 0.6$ and $x_b = 0.95$ for the right rarefaction wave. Table 2 shows the L_1 norm of error along with the order of convergence for the four versions of the GFM, where the results from the EGFM-V2 and OGFM have the lowest and largest errors respectively, while the error from the RGFM and the EGFM-V1 are comparable. As explained in observation 6 in §4.1, assigning interfacial values U_{*L} and U_{*R} directly to the cells next to the interface causes this error in the RGFM and the EGFM-V1 results, while the EGFM-V2 resolves this issue efficiently, leading to the minimum error in capturing the wave location. However, it is seen that the order of convergence for all methods is near unity, except for that from the OGFM, where the convergence rate is 0.84 for the finest mesh.

7.1.3. Multi-component shock tube problem with strong pressure jump [36]

This is an MMRP where a diaphragm separates two gases ($\gamma_L = 1.6$ and $\gamma_R = 1.4$) in the domain. The initial discontinuity is located at the center ($x_0 = 0.5$) of the shock tube and separates regions with a pressure ratio of 2500:1. The initial data is summarized as

$$W_L = (\rho_L, u_L, p_L) = (1, 0, 500),$$

$$W_R = (\rho_R, u_R, p_R) = (1, 0, 0.2).$$

The solution [36] includes a left rarefaction and a right shock as shown for $t = 0.01$ in Fig. 9 with 80 cells used in the computational domain with $CFL = 0.3$. However, to obtain the results using the OGFM, the CFL value must be reduced to ≤ 0.04, indicating the approach is not ideal for this MMRP. Moreover, it is seen that the OGFM captures the interface three cells away from its actual position (see the discussion of Problem 7.1.2 for the details of such behavior) and exhibits large errors near the rarefaction corner and the interface in the temperature profile. The RGFM, in contrast, captures the interface at the correct location with smaller overheating errors. Fig. 9 shows that the results from the EGFM are of higher accuracy, and overheating has been eliminated in both versions; the erroneous feature near the rarefaction corner has been removed and the wave locations are more accurate. This is seen in Table 3, where the error from the EGFM-V2 is minimum, while the OGFM creates the highest error in the rarefaction location ($x_a = 0.15$ and $x_b = 0.45$). As observed for Problem 7.1.2, the error from the RGFM and the EGFM-V1 are similar, with the latter being slightly more accurate. Despite the error magnitude, it is seen that the order of convergence is near unity for all versions.

7.1.4. Strong shock impacting on a gas-water interface (heavy → light) [7]

In this non-dimensional example, the domain is occupied by air ($\gamma_L = 1.4$) and water ($\gamma_R = 4$ and $p_{\infty R} = 1$), where the two materials are separated by an interface at $x_0 = 0.5$. A left-traveling shock of strength $M_S = 1.95$ is initialized at $x_{S0} = 0.6$ in the water region of the shock tube and traverses the interface. The complete initial data for this problem is

$$W_L = (\rho_L, u_L, p_L) = (1, 0, 1),$$

$$W_R = (\rho_R, u_R, p_R) = (5, 0, 1),$$

$$W_S = (\rho_S, u_S, p_S) = (7.093, -0.7288, 10),$$

where W_S represents the post-shock state. Since this is a heavy-to-light case, a rarefaction is reflected back into the water, while a shock is transmitted into the air. Fig. 10 shows the analytical solution, as well as

Table 2
The L_1 norm of error in density for the right rarefaction wave in Problem 7.1.2. The error is minimum for the EGFM-V2, while the order of convergence is similar for the MMRP-based GFMs.

No. of cells	OGFM		RGFM		EGFM-V1		EGFM-V2	
	L_1	Order	L_1	Order	L_1	Order	L_1	Order
80	0.0195		0.0177		0.0141		0.0068	
128	0.0148	0.5868	0.0117	0.8808	0.0090	0.9552	0.0043	0.9751
200	0.0109	0.6853	0.0079	0.8800	0.0058	0.9845	0.0028	0.9613
320	0.0080	0.6581	0.0051	0.9311	0.0037	0.9564	0.0017	1.0617
500	0.0055	0.8396	0.0034	0.9085	0.0024	0.9699	0.0011	0.9754

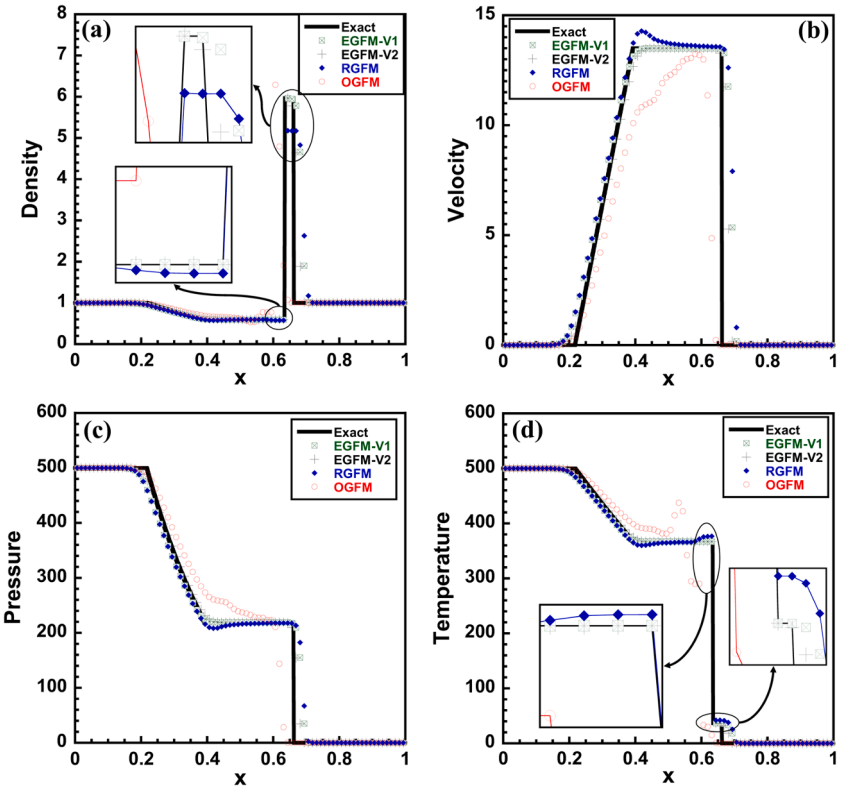

Fig. 9. The numerical solutions of Problem 7.1.3 by the OGFM, RGFM, EGFM-V1, and EGFM-V2 compared to the exact solution for (a) density, (b) velocity, (c) pressure, and (d) temperature. The EGFM-V1 and EGFM-V2 completely remove overheating and capture the waves more accurately.

Table 3
The L_1 norm of error in density for the left rarefaction wave in Problem 7.1.3. The OGFM and the EGFM-V2 have the highest and the lowest errors, respectively. The order of convergence is unity for all versions.

No. of cells	OGFM		RGFM		EGFM-V1		EGFM-V2	
	L_1	Order	L_1	Order	L_1	Order	L_1	Order
80	0.0448		0.0197		0.0155		0.0079	
128	0.0319	0.7226	0.0127	0.9341	0.0096	1.0193	0.0048	1.0601
200	0.0224	0.7922	0.0086	0.8735	0.0063	0.9438	0.0031	0.9797
320	0.0146	0.9107	0.0056	0.9128	0.0040	0.9665	0.0020	0.9325
500	0.0095	0.9629	0.0037	0.9286	0.0025	1.0531	0.0013	0.9653

a comparison between the OGFM, RGFM, and EGFM approaches at $t = 0.2$. All the simulations shown in Fig. 10 were performed with a mesh of 128 cells and $CFL = 0.2$. Note that in Fig. 10(d), the plot indicates the temperature of the air for $x \in [0, 0.305)$ and the internal energy of the water for $x \in (0.305, 1]$.

The introduction of the initial shock wave as a perfectly sharp discontinuity in the water leads to the formation of two spikes in the solution propagating throughout the domain in time. However, these features (located at $x \sim 0.4$ and $x \sim 0.95$ at the end of the simulation) are removed by the shock treatment in the EGFM approach (§5) as seen in the insets in Fig. 10(c)–(d). In addition, the EGFM eliminates overheating near the interface, as shown in detail in Fig. 10(a) and (d). Finally, the L_1 norm of error in density is computed for the right rarefaction for $x_a = 0.55$ and $x_b = 0.83$. As seen in Table 4, and unlike the previous cases, the OGFM has lower errors compared to the RGFM and EGFM-V1. However, the EGFM-V2 has the least error among all versions, indicating that this particular algorithm is highly accurate in capturing the waves in shock-interface interactions.

7.1.5. Strong shock impacting on a gas-gas interface (heavy → light) [11]

In this problem, we investigate the performance of the EGFM in removing overheating, when used in conjunction with an ARS or in the presence of numerically diffuse shocks. For brevity, only the density results are shown, while similar trends were observed in the temperature and entropy plots. The computational domain contains left ($\gamma_L = 1.6667$) and right ($\gamma_R = 1.4$) gases separated by an interface located at $x_0 = 0.2$. A right-travelling shock initially positioned at $x_{S0} = 0.05$, divides the left gas into pre- and post-shock regions. The initial conditions for the problem are given by

$$W_S = (\rho_S, u_S, p_S) = (3.86, 8.56, 100),$$

$$W_L = (\rho_L, u_L, p_L) = (1, 0, 1),$$

$$W_R = (\rho_R, u_R, p_R) = (0.1, 0, 1).$$

Fig. 11 compares the exact solution at $t = 0.05$ with the numerical solutions obtained using 100 cells with $CFL = 0.3$ from six different approaches: (1) EGFM-V1 with shock treatment (§5), (2) EGFM-V1 with a diffuse shock (DS EGFM-V1), (3) the 2D version of the EGFM-V1 (2D EGFM-V1) (§6), (4) EGFM-V1 coupled with linearized Riemann solver [37] (LRS) (EGFM-V1 LRS), (5) the RGFM, and (6) the OGFM. Fig. 11 indicates that approximate versions of the EGFM exhibit slight overheating errors near the interface. Note that in approaches (2) and (3), the shock is allowed to diffuse before impacting the interface. Fig. 11

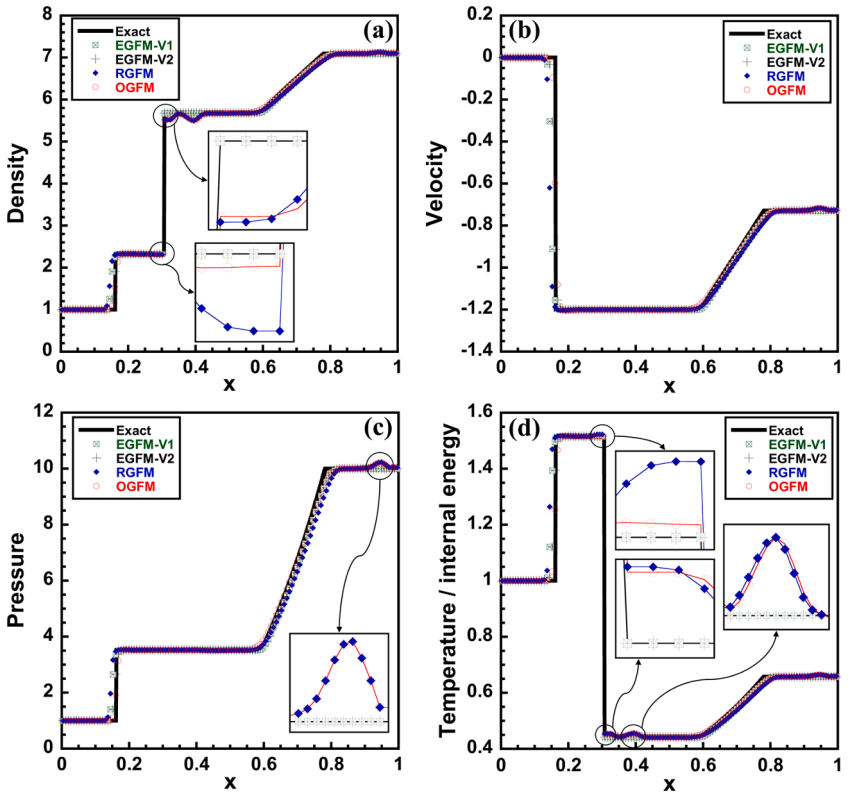

Fig. 10. The numerical solutions of Problem 7.1.4 by the OGFM, RGFM, EGFM-V1, and EGFM-V2 compared to the exact solution for (a) density, (b) velocity, (c) pressure, and (d) temperature/internal energy. The shock treatment in §5 removes the erroneous features at $x \sim 0.4$ and $x \sim 0.95$. The EGFM versions eliminate overheating in the density, temperature, and internal energy profiles.

Table 4
The L_1 norm of error in density for the right rarefaction wave in Problem 7.1.4. The EGFM-V2 has the lowest error in capturing the wave in the water. The order of convergence is near unity for all versions in this shock-interface interaction problem.

No. of cells	OGFM		RGFM		EGFM-V1		EGFM-V2	
	L_1	Order	L_1	Order	L_1	Order	L_1	Order
80	0.0441		0.0908		0.0470		0.0368	
128	0.0273	1.0204	0.0587	0.9281	0.0323	0.7980	0.0260	0.7391
200	0.0197	0.7311	0.0439	0.6510	0.0245	0.6193	0.0193	0.6677
320	0.0123	1.0022	0.0273	1.0107	0.0157	0.9468	0.0118	1.0468
500	0.0079	0.9920	0.0175	0.9964	0.0100	1.0107	0.0075	1.0155

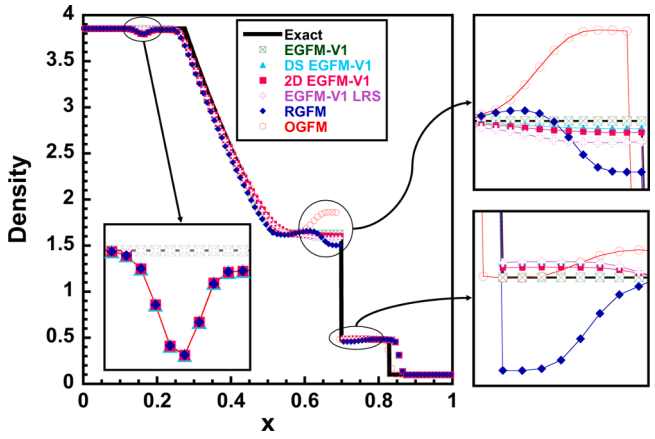

Fig. 11. Density profile from problem 7.1.5 obtained from EGFM-V1, EGFM-V1 with diffuse shock (DS EGFM-V1), 2D version of the EGFM-V1 (2D EGFM-V1), EGFM-V1 with linearized Riemann solver (EGFM-V1 LRS), RGFM, and OGFM.

shows the EGFM-V1 is in very good agreement with the exact solution. The corresponding 2D implementation was computed without a sharp representation of the shock in the current work, which leads to slight deviations from the exact solution. Similarly, when the EGFM is computed with a diffuse shock representation (DS EGFM-V1) or using the LRS (EGFM-V1 LRS), slight overheating errors are observed as seen in Fig. 11. However, these approximate implementations of the EGFM still significantly outperform the RGFM and OGFM near the interface. The RMS error from the different implementations were computed over 20 cells (10 cells on each side of interface) and determined to be 0.01186, 0.01752, 0.03423, 0.06167, and 0.28590 for DS EGFM-V1, 2D EGFM-V1, EGFM-V1 LRS, RGFM, and OGFM, respectively. In addition, all MMRP-based versions of the GFM capture the interface at the correct location, while the interface from the OGFM is one cell away. Finally, note that in the approaches where the initial shock is allowed to diffuse, a spurious numerical oscillation is observed at $x \sim 1.7$.

7.2. 2D test problems

In this section, we use the EGFM 2D algorithm described in §6 in the simulation of the following test problems; Sod problem with radial

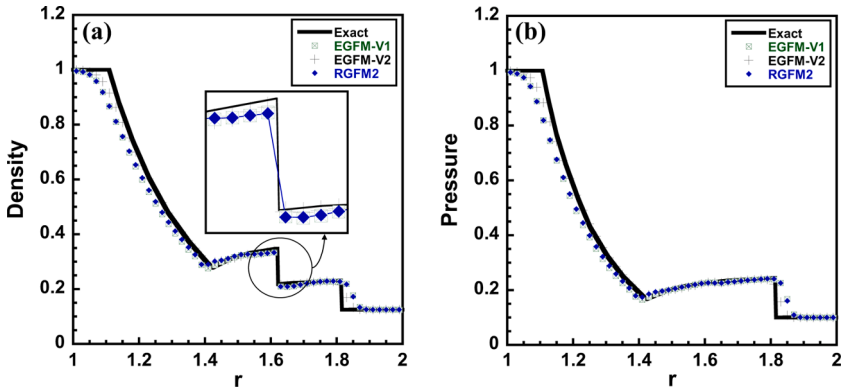

Fig. 12. (a) Density and (b) pressure profiles for the radial Sod problem along $y = 1$ and $1 \leq r \leq 2$ using the RGFM2, EGFM-V1, and EGFM-V2. The EGFM-V2 reduces overheating errors near the radial contact discontinuity and captures the waves at their correct locations.

symmetry, shock-air cavity interaction, and RM instability with and without surface tension. For problems involving shock-interface interaction, we will only present the results from the EGFM-V1. Our simulations show that this version results in more accurate solutions near the interface in such problems.

7.2.1. Sod problem with radial symmetry [26]

In this problem, the computational domain is a square of size $[0, 2] \times [0, 2]$ in the xy plane containing a region of low pressure ($\rho = 0.125$ and $p = 0.1$) air ($\gamma = 1.4$) surrounding a circular bubble containing high-pressure ($\rho = 1$ and $p = 1$) air with a radius of 0.4 and centered at (1,1). The simulation was run to a final time of $t = 0.25$ using a mesh of 100×100 cells and $CFL = 0.3$. Fig. 12 shows the 1D density and pressure profiles along $y = 1$ and $1 \leq r \leq 2$ obtained using different MMRP-based GFM versions. All three methods are consistent with the exact solution [26], which predicts an inward-propagating rarefaction and an outward-traveling shock wave. Near the contact wave, similar overheating errors are observed in the simulations employing RGFM2 and EGFM-V1, while the EGFM-V2 mitigates these errors and results in a more accurate solution. Furthermore, both the EGFM-V1 and RGFM2 place the rarefaction and the shock waves ahead of their actual locations, while the EGFM-V2 computes the correct locations of the waves. Similar to the 1D cases, we compute the L_1 norm of error in density for the rarefaction on $[r_a, r_b]$ where $r_a = 1$ and $r_b = 1.5$, to compare the performance of each version in capturing the wave, as seen in Table 5. The errors from the EGFM-V1 and RGFM2 are similar, while the EGFM-V2 approach reports much lower values of the L_1 error. However, it is seen from Table 5 that the order of convergence approaches unity for all three versions.

Table 6 is a comparison of the total simulation time for both versions of the EGFM and the RGFM2 approach. Similar to other GFM approaches, the EGFM is only computed for cells within the computational stencil straddling the interface. For a material interface that is resolved by N points in a simulation, all the GFM-based approaches will require

Table 5
The L_1 norm of error in density for the inward rarefaction wave in Problem 7.2.1. The error is computed on $r \in [1, 1.5]$ between the center of the domain $(1, 1)$ and $(1.5, 1)$. The EGFM-V2 has the lowest error in capturing the wave. The order of convergence is near unity for all versions in this radial problem.

No. of cells	CFL No. [30]	RGFM2 L_1	Order	EGFM-V1 L_1	Order	EGFM-V2 L_1	Order
32	0.5	0.1525		0.1411		0.0495	
50	0.4	0.0892	1.2017	0.0922	0.9534	0.0257	1.4687
100	0.3	0.0395	1.1752	0.0413	1.1586	0.0124	1.0514
200	0.2	0.0234	0.7553	0.0240	0.7831	0.0068	0.8667
320	0.2	0.0162	0.7824	0.0161	0.8494	0.0044	0.9262

Table 6
Simulation time (CPU time in seconds) for different versions of the GFM.

No. of cells	CFL No. [30]	RGFM2	EGFM-V1	EGFM-V2
32	0.5	4.12	4.12	4.12
50	0.4	8.33	8.35	8.35
100	0.3	44.95	45.37	45.39
200	0.2	302.19	310.41	310.98
320	0.2	983.41	1060.12	1065.12

$O(N)$ operations, with slight variations in computational effort that appear to be resolution-dependent in Table 6 (at the highest resolution investigated, the EGFM approaches were less than $\sim 10\%$ more expensive than RGFM2). The comparison in Table 6 was based on maintaining the same CFL numbers across all methods. Since the EGFM has been shown to be a more accurate and stable method (see Fig. 13), the slight increase in computational effort can be offset by performing simulations at an appropriately lower resolution and by choosing larger CFL numbers.

In Fig. 13, the interface ($\phi = 0$) from the three methods is plotted at the end of the simulation. In this figure, numerical oscillations and small-amplitude wiggles are observed in RGFM2, specifically near the horizontal and vertical poles. As discussed in [26], these oscillations are due to the "staircase" representation of the initial discontinuity at the beginning of the simulation. In contrast, the EGFM versions mitigate these errors at the contact wave; in particular, the EGFM-V1 reduces the amplitude of the oscillations, while the EGFM-V2 completely removes the wiggles, resulting in a smooth interface with a perfectly radial shape. The observed higher accuracy in capturing the waves (Table 5) and interfaces (Fig. 13) demonstrates the effectiveness of the EGFM approach, while highlighting the importance of applying the isentropic fix *after* the solution from the single-medium solvers are obtained.

In Fig. 14, the numerical solutions for density are plotted for three different mesh sizes for RGFM2 and EGFM-V2: 100×100, 200×200, and 320×320 cells. For both methods, overheating errors improve with resolution, but persistent overheating is observed for RGFM2 even at the highest resolution. In contrast, for EGFM-V2 the errors from overheating $\to 0$ rapidly with decreasing mesh width (a slight trough seen in the EGFM solution at resolution of 200 cells is attributed to not applying the correction to the cells further away from the interface). In the current implementation of EGFM in multi-dimensions, this issue can be remedied by refining the mesh selectively in regions with locally large curvature such as kinks, pinch-off points etc. A multi-dimensional implementation of the EGFM that is exact in cells further from the interface will include the source terms in Eq. (18), and will be discussed in a future publication.

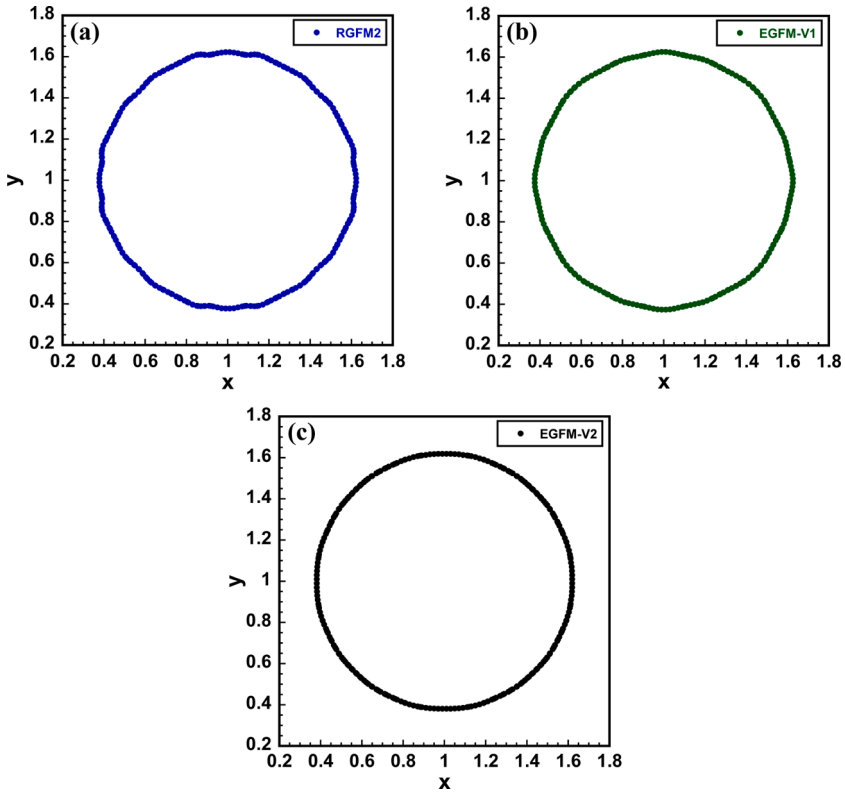

Fig. 13. The contact wave location ($\phi = 0$) from (a) the RGFM2, (b) the EGFM-V1, and (c) the EGFM-V2. Numerical errors at the interface are observed due to the "staircase" effect associated with the representation of the initial discontinuity at the beginning of the simulation. The EGFM-V1 reduces the amplitude of the numerical oscillations, while the EGFM-V2 results in a smooth radial contact wave free of the numerical wiggles.

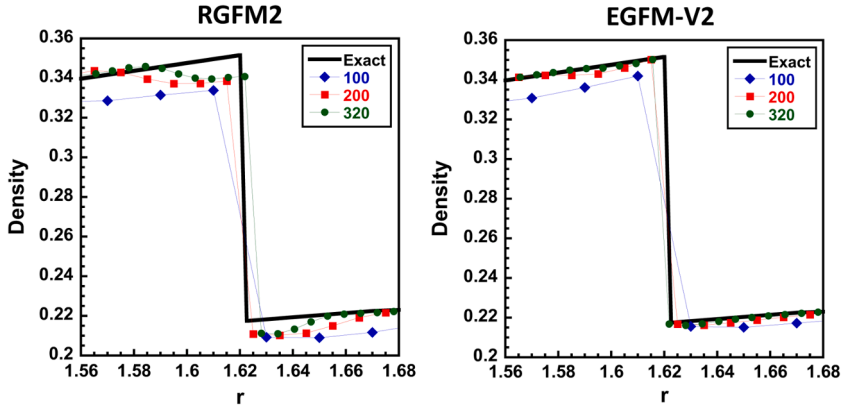

Fig. 14. Plots of density near the contact discontinuity in the radial Sod problem for RGFM2 (left) and EGFM-V2 (right) approaches. The overheating errors persist in the RGFM2 solution, while vanishing in the limit of $\kappa\Delta x \to 0$ for EGFM-V2.

7.2.2. Strong shock-air cavity interaction (heavy → light) [38]

This demanding problem has been investigated in previous studies [20,38–44], and used here to demonstrate the performance of the EGFM for shock-interface interactions with large density ratios. The problem consists of a square domain of dimensions $[0,2] \times [0,2]$ mm^2 filled with water ($\gamma_w = 4.4$ and $p_{\infty w} = 6 \times 10^8$ Pa) surrounding a circular cavity of diameter 1 mm centered at (1 mm, 1 mm) and filled with air ($\gamma_a = 1.4$). A right-traveling shock wave of strength $M_S = 1.43$, and initially located at $x_{S0} = 0.4$ mm, divides the water region into post-shocked and pre-shocked states, and approaches the air cavity from the left. The initial conditions of the problem with the *post-* and *pre-* suffixes for the water are as follows:

$$W_{w,post} = (\rho, u, v, P)_{w,post} = \left(1233.4 \text{ kg}/\text{m}^3,\ 439.8 \text{ m}/\text{s},\ 0,\ 1.02 \times 10^9 \text{ Pa}\right),$$

$$W_{w,pre} = (\rho, u, v, P)_{w,pre} = \left(1000 \text{ kg}/\text{m}^3,\ 0,\ 0,\ 10^5 \text{ Pa}\right),$$

$$W_a = (\rho, u, v, P)_a = \left(1 \text{ kg}/\text{m}^3,\ 0,\ 0,\ 10^5 \text{ Pa}\right).$$

This is a challenging problem since the initial density ratio at the interface is large (1000:1), while the pressure behind the shock is in *GPa*. In this problem, we employ AMR with three levels of refinement with the finest mesh size corresponding to $1/256$ mm ($CFL = 0.4$), while the simulation is run to a final time of $t = 731.85$ ns. The left and right boundaries are outflow surfaces to avoid any reflections back into the

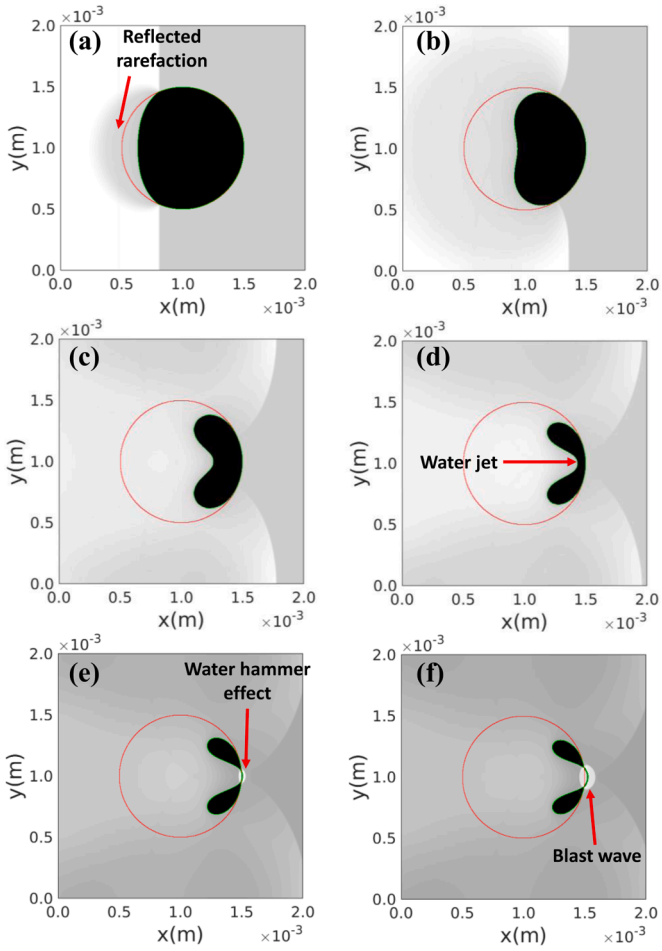

Fig. 15. Evolution of the interface in the water-air shock-cavity interaction problem for t_c = (a) 136.54 ns, (b) 373.51 ns, (c) 554.89 ns, (d) 638.71 ns, (e) 675.65 ns, and (f) 693.13 ns. The initial cavity has been shown by the red solid line in all plots. Figs. 15(a),(b) show the formation and propagation of the waves resulting from the interaction, while Figs. 15(c),(d) demonstrate the evolution of the water jet. Fig. 15(e) indicates the formation of the blast wave and the "water hammer" effect, and Fig. 15(f) illustrates the propagation of the blast wave along with the interface division into two smaller interfaces. (For interpretation of the references to color in this figure legend, the reader is referred to the web version of this article.)

domain, while the top and bottom boundaries are periodic. In order to quantitatively compare our results with those from [42,43], we use the time scale $t_c = t - t_0$, where $t_0 = 38.72\ ns$ is the time it takes the shock wave to reach the cavity.

The density plots of the flow field are seen in Fig. 15 for different t_c, and demonstrate key features of the flow and the interface evolution in time. Since this is a heavy-to-light case, upon the shock-interface interaction (Fig. 15(a)), the initial shock wave is refracted to a reflected rarefaction wave into the water and a transmitted shock wave into air. Figs. 15(c)–(d) illustrate the formation and development of a water jet into the air cavity, where the air is highly compressed as the jet evolves to the right. Fig. 15(e) corresponds to the time when the left and right surfaces of the air cavity meet, and a strong blast wave is initiated, and a "water hammer" effect [20] is observed. As the high-speed water jet impacts the stationary surface of the air cavity, the subsequent splitting of the initial interface is accurately captured by the numerical method. Eventually, the blast wave creates a high-density, high-pressure region at the tip of the water jet, which propagates radially in all directions, as seen in Fig. 15(f). Thus, Fig. 15 demonstrates the ability of the EGFM approach to handle strong shock interactions in problems with large density differences.

Table 7
A comparison between the results from the simulation and those from previous studies shows a close agreement between the three different approaches.

Parameter	Hawker and Ventikos [43]	Bempedelis and Ventikos [42]	EGFM-V1
First stage time (ns)	675	680	669
Jet speed at impact (m/s)	2278	2131	2110
Water hammer pressure (Gpa)	3.00	3.48	3.14

In Table 7, the first stage time, the jet speed at impact, and the water hammer pressure are compared with the results from a previously studied front tracking method [43], and recently studied grid-aligned GFM [42]. The first stage time is measured using t_c and is defined as the time interval between the first shock-cavity interaction, and when the two horizontal poles of the cavity meet. Table 7 indicates there is close agreement between the three different approaches, and further validates the EGFM capabilities to simulate flows with highly stiff materials under high-speeds and high-pressure conditions.

7.2.3. *Richtmyer–Meshkov instability (light → heavy)*

The single-mode RM [22,23] instability is investigated in this section. The problem setup is as shown in Fig. 16, and involves a rectangular domain of dimensions $L_x \times L_y$ with an interface represented by $x = x_0 + h_0^- \cos(2\pi y/\lambda)$, where x_0 is the location of the unperturbed interface, h_0^- is the amplitude of the perturbation before shock impact, and λ is the perturbation wavelength.

The problem statement is summarized in Fig. 16, which shows the simulation domain occupied by Fluids A and B, where Fluid A supports a planar shock wave traveling toward the interface with speed S. The density contrast between the two fluids is characterized by the pre-shock Atwood number $A^- = (\rho_B - \rho_A)/(\rho_B + \rho_A)$, where $A^- > 0$ indicates a light-to-heavy interaction. The amplitude of the perturbation has been scaled by the wavenumber to define the nondimensional parameter kh_0^-, where $k = 2\pi/\lambda$ is the perturbation wavenumber. The shock Mach number is defined as $M_S = S/a_A$, where a_A is the speed of sound in Fluid A in its unshocked state.

The simulations were performed with air and SF_6 as the two fluids separated by the initial interface, and labeled as Fluid A ($\gamma_A = 1.4$) and Fluid B ($\gamma_B = 1.093$), respectively. We use $\rho_A = 0.5\ \mathrm{kg/m^3}$ and $\rho_B = 2.5\ \mathrm{kg/m^3}$ corresponding to $A^- = \frac{2}{3}$. The initial interface perturbation is characterized by the pre-shock amplitude $h_0^- = 0.056$ m, and a perturbation wavelength $\lambda = 1$ m, so that $kh_0^- = 0.35$. A planar shock with $M_S = 1.2$ was initialized at $x_{S0} = 0.4$ m, while the interface was positioned at $x_0 = 0.5$ m. The initial condition for the problem is detailed below, with the *post-* and *pre-*suffixes indicating post-shocked and pre-

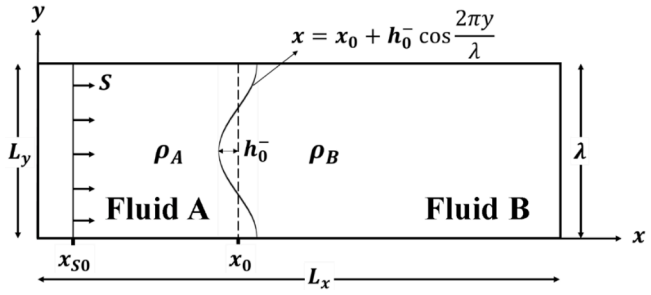

Fig. 16. Problem setup for the RM instability simulation. The domain size is $L_x \times L_y$, and the interface between Fluids A and B is defined as a single-mode perturbation represented by a cosine wave of wavelength $\lambda = L_y$. The dashed line shows the unperturbed interface. The right-traveling shock of speed S is initially located at x_{S0} and impacts the perturbed interface between the fluids.

shocked states respectively:

$$W_{A,post} = (\rho, u, v, P)_{A,post} = \left(0.67\ \text{kg}/\text{m}^3,\ 161.68\ \text{m}/\text{s},\ 0,\ 1.5\ \times 10^5\ \text{Pa}\right),$$

$$W_{A,pre} = (\rho, u, v, P)_{A,pre} = \left(0.5\ \text{kg}/\text{m}^3,\ 0,\ 0,\ 10^5\ \text{Pa}\right),$$

$$W_B = (\rho, u, v, P)_B = \left(2.5\ \text{kg}/\text{m}^3,\ 0,\ 0,\ 10^5\ \text{Pa}\right).$$

The simulation domain had dimensions of $L_x = 10$ m and $L_y = 1\ m$. AMR with three levels of refinement was used, with the finest mesh corresponding to a resolution of $1/256$ m. The simulations were performed with $CFL = 0.6$, and to a final time of $t = 0.078$ s. The left and right boundaries were treated as outflow surfaces to allow for the egress of waves without acoustic feedback into the domain, while the top and bottom boundaries were defined using periodic boundary conditions.

Upon passage of the shock through the interface, the interface is accelerated to a velocity Δv and compressed to a post-shock amplitude h_0^+ with a compression factor $\chi = h_0^+/h_0^-$. Under the influence of the deposited baroclinic vorticity, the perturbation amplitude grows in time with a growth rate $V_{RM} = dh/dt$. In Table 8, we compare the results from the EGFM-V1 with predictions from the Rankine–Hugoniot relations applied to the RM situation [45,46], and with analytical models for the RM linear growth rate [22,23]. Table 8 shows excellent agreement between model predictions and measured quantities from simulations using the EGFM-V1 during the linear stage of RM instability growth.

In Fig. 17, we plot two sets of numerical Schlieren images at different nondimensional times kV_0t, where V_0 is the initial growth rate that accounts for finite-amplitude effects and is given by $V_0 = V_{RM}/[1+(kh_0^-/3)^{4/3}]$ [47]. Fig. 17(a) shows the interface during its linear evolution, while figures (b)–(d) show the interface growth during the nonlinear stages ($kV_0t \gtrsim 1$). Since this is a light-to-heavy case, the incident shock upon impinging on the interface is refracted into a shock reflected back through air, and a transmitted shock into SF_6. Fig. 17(a) shows the interface after passage of the shock, maintaining its sinusoidally symmetric shape about the unperturbed interface, shown as the dashed line. However, at late times ($kV_0t \gtrsim 1$), higher harmonics [47] are dominant leading to the appearance of distinct spike and bubble structures.

A branched simulation in which the interface was shocked a second time, by a shock reflected from the domain boundary was performed. We plot Schlieren images of the interface for this problem in Fig. 17(e)–(h). Since this second shock-interface interaction is a slow/fast interaction, the interface undergoes a reversal in sign, where former bubble structures have now formed spikes and vice versa. Furthermore, since the interface was already nonlinear at the time of reshock, significant baroclinic vorticity is deposited during this interaction, leading to the complex features seen in Fig. 17(g),(h). At late times ($kV_0t = 10$), slight asymmetry in the flow structures is observed, similar to previous studies of RM instabilities [47].

The growth in time of the bubble and spike amplitudes (h_{bu} and h_{sp} in Fig. 17(a)–(d)) are shown in Fig. 18(a), where they have been normalized by the post-shock initial amplitude h_0^+. Consistent with the large density ratio used in the simulations, spikes and bubbles exhibit asymmetric growth, with the spike outpacing the bubble growth [48–53]. The amplitudes are compared with predictions from the nonlinear model of Dimonte and Ramaprabhu [47] (D&R), where the bubble and spike growth rates V_{bu} (dh_{bu}/dt) and V_{sp} (dh_{sp}/dt) are predicted as:

$$V_{bu/sp} = V_0 \frac{1 + (1 \mp |A^+|)kV_0t}{1 + C_{bu/sp}kV_0t + (1 \mp |A^+|)F_{bu/sp}(kV_0t)^2}, \tag{19}$$

and the coefficients F and C are, respectively defined as:

$$F_{bu/sp} = 1 \pm |A^+|, \tag{20}$$

$$C_{bu/sp} = \frac{4.5 \pm |A^+| + (2 \mp |A^+|)\left|kh_0^+\right|}{4}. \tag{21}$$

Eq. (19) has been numerically integrated to obtain the model curves in Fig. 18(a). The simulation results are in excellent agreement with the model for spike and bubble amplitudes throughout their evolution. In Fig. 18(b), we also compare the growth rates from Eq. (19) with the corresponding bubble and spike growth rates from the EGFM-V1. From this figure, spike and bubble velocities from EGFM-V1 are in very good agreement with the nonlinear model of Dimonte and Ramaprabhu [47].

7.2.4. Richtmyer–Meshkov instability under the effect of surface tension

The problem configuration follows Problem 7.2.3, but with surface tension effects included at the interface (for additional validation problems with surface tension, see [24]). Surface tension, as explained in §2, is handled numerically using $\Delta p = \sigma\kappa$ directly in the multi-medium Riemann solver at the interface. In this section, the effect of surface tension on the linear growth of RM instability is described using the results from IMPACT simulations. In the linear regime, surface tension stabilizes RM instability as predicted by the model of Mikaelian [54], and results in an oscillatory behavior of the interface about its mean (unperturbed) position.

The analytical model by Mikaelian [54] applies to a single-mode RM instability, and predicts the time dependence of the amplitude of a perturbed interface with imposed surface >tension:

$$\frac{h(t)}{h_0^+} = \cos\omega t + \frac{\Delta v k A^+}{\omega}\sin\omega t\ . \tag{22}$$

In Eq. (19), ω is the angular frequency of surface tension-driven oscillations and given by

$$\omega = \sqrt{\frac{k^3\sigma}{\rho_A^+ + \rho_B^+}}, \tag{23}$$

where ρ_A^+ and ρ_B^+ are the post-shock values of densities on either side of the interface (see Fig. 16). From Eq. (22), the maximum perturbation amplitude [54] is obtained as:

$$h_{max} = h_0^+\sqrt{1 + \left(\frac{kA^+\Delta v}{\omega}\right)^2}. \tag{24}$$

Using Eqs. (23),(24), we estimate a lower limit for the surface tension to ensure $kh_{max} \leq 1$ in our simulations, so that perturbation amplitudes in the IMPACT simulations stayed within the linear regime, where the above model is applicable. Using $\rho_A^+ = 0.737\ \text{kg}/\text{m}^3$ and $\rho_B^+ = 4.109\ \text{kg}/\text{m}^3$ from Problem 7.2.3, and the post-shock values from Table 8, we estimate for the parameters of the problem, the RM instability will remain in the linear regime for $\sigma \gtrsim \sigma_{crit} = 400\ N/m$. Thus, for $\sigma \gtrsim \sigma_{crit}$, results from the IMPACT simulations can be compared with the model Eqs. (22)–(24).

The evolution of the interface for $\sigma = 400$ N/m is shown in Fig. 19,

Table 8
A comparison of the results from theoretical models of the linear growth of RM instability with results from the simulations.

Quantity	Parameter	Theory	EGFM-V1
Interface velocity	Δv (m/s)	106.58 ([45,46])	107.01
Post-shock Atwood number	A^+	0.696 ([45,46])	0.696
Post-shock interface perturbation amplitude	h_0^+ (m)	0.0464 ([23])	0.0465
Amplitude compression ratio	χ	0.832 ([23])	0.834
Initial (linear) perturbation growth rate	$dh/dt \equiv V_{RM}$ (m/s)	21.605 ([22])	21.753

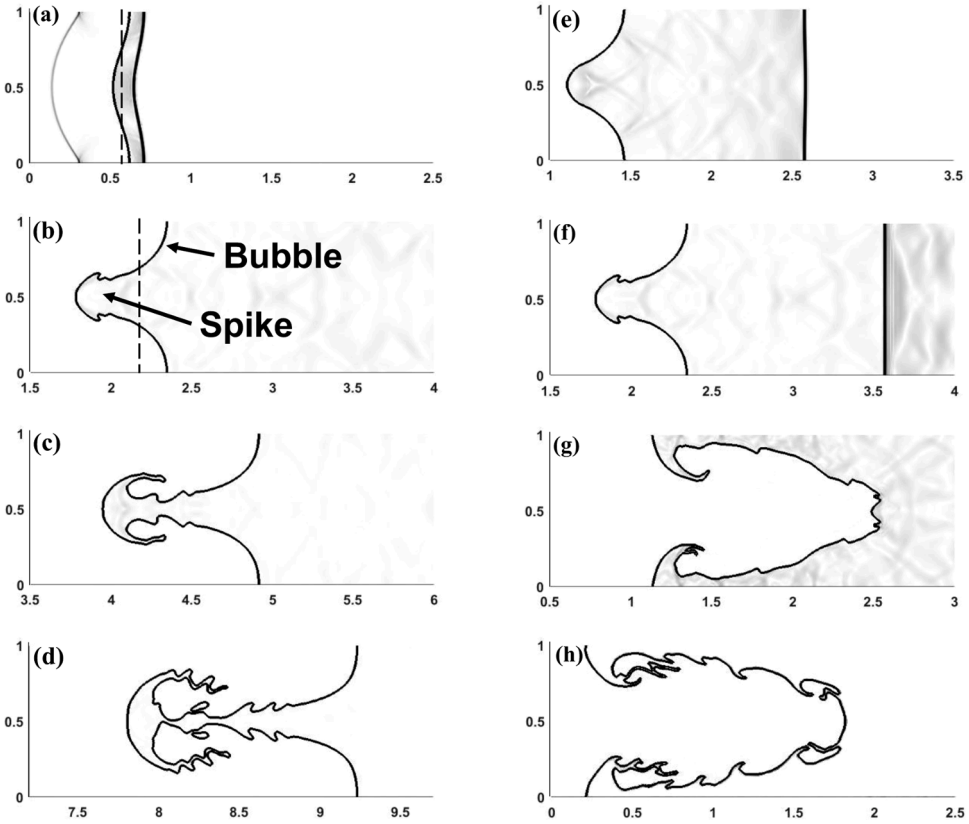

Fig. 17. Schlieren images of the interface evolution in the RM instability problem. Left column: the growth of spike and bubble (the dashed line indicates unperturbed interface) for $kV_0t =$ (a) 0.1, (b) 2.0, (c) 5.0, (d) 10.0. Right column: the reshock problem for $kV_0t =$ (e) 1.0, (f) 2.0, (g) 5.0, and (h) 10.0.

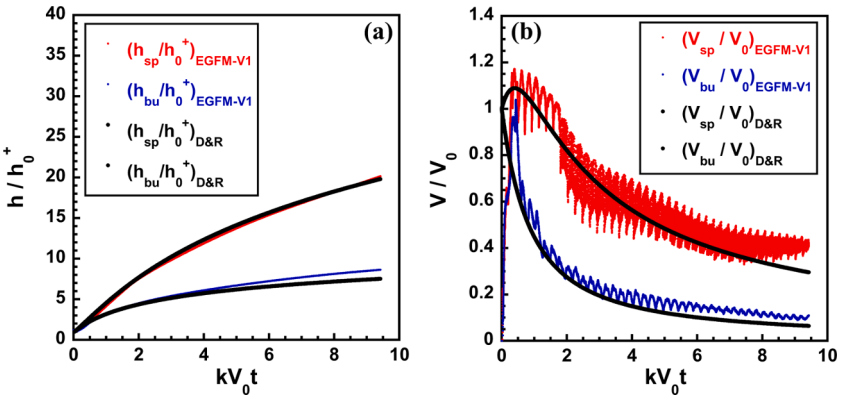

Fig. 18. (a) Time evolution of spike and bubble amplitudes from the EGFM-V1. (b) Time evolution of spike and bubble growth rates. Results from the EGFM-V1 are compared with the nonlinear model of Dimonte and Ramaprabhu [47]. The spike and bubble amplitudes and growth rates are in excellent agreement with the model.

and exhibits an oscillatory behavior in contrast to Problem 7.2.3. The corresponding amplitude evolution is shown in Fig. 20. Following an initial compression of the pre-shock amplitude h_0^- to h_0^+ visible in Fig. 20 at $kV_0t \sim 0$, an oscillatory behavior is established. As seen in this figure, increasing σ results in oscillations with lower peak amplitudes but with higher frequencies, as predicted by Eqs. (23), (24). The values of σ in this figure have been chosen such that the interface undergoes at least 1, 3, and 5 full cycles in the oscillations for $0 \leq kV_0t \leq 10$. Note that the slight attenuation in the maximum amplitude is attributed to numerical diffusion (see [39,55] for a similar behavior in simulations involving surface tension). Finally, we compare the periods of oscillations and maximum amplitudes from our simulations with those predicted by the model of Mikaelian [54] over a wide range of surface tension coefficients in Fig. 21. In this figure, we see that there is excellent agreement between the simulation results and the analytical model for both the time period of oscillations and the peak amplitudes. In Fig. 21 (b), h_{max} from IMPACT is slightly lower than the model, due to numerical diffusion from the finite mesh. The overall excellent agreement between the simulations and the model shows the EGFM approach is successful in capturing surface tension effects for multi-material problems.

8. Conclusions

In this paper, a new version of the GFM termed the Efficient Ghost Fluid Method (EGFM) has been proposed, and is capable of completely eliminating overheating errors from fluid interfaces in compressible multi-medium flows. Previous efforts aimed at containing overheating errors (such as the isentropic fix), did not completely eliminate the

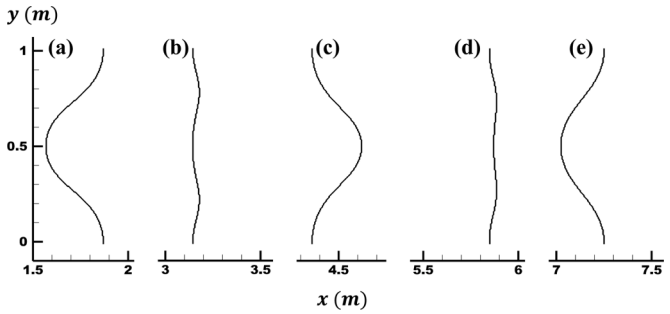

Fig. 19. The interface location at t = (a) 0.0115 s, (b) 0.0229 s, (c) 0.0342 s, (d) 0.0458 s, and (e) 0.0571 s from the RM simulations evolving under the effect of surface tension with $\sigma = 400$ **N/m**. The chosen times approximately correspond to (a) $T/4$, (b) $T/2$, (c) $3T/4$, (d) T, and (e) $5T/4$, where T is the period of oscillations from Eq. (23).

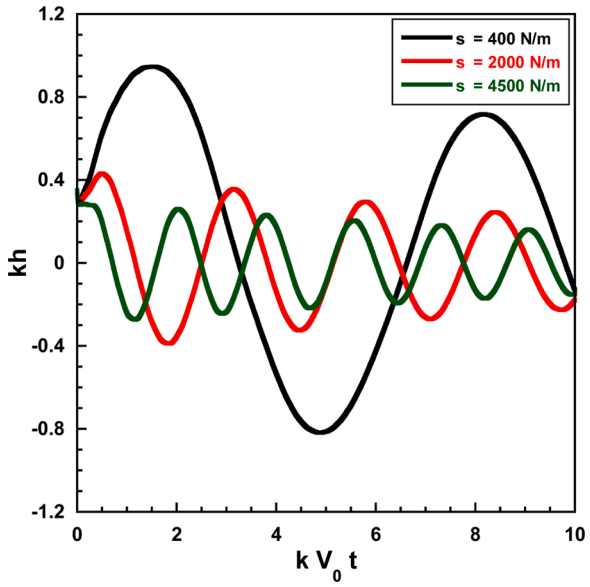

Fig. 20. Time evolution of the perturbation amplitude corresponding to different values of surface tension. Higher σ leads to higher frequencies, yet limits the peak amplitudes, in agreement with the model Eqs. (23),(24).

numerical artifact, although the errors were mitigated to some extent. Through detailed numerical simulations of several test problems, we have demonstrated that the proposed approach is successful at eliminating overheating.

The EGFM was implemented in IMPACT, a shock physics code developed for the simulation of compressible multi-medium flows, and validated by simulating several standard and demanding 1D problems. These include single- and multi-medium Riemann problems, shock impedance matching problems, and shock-interface interactions. When compared with the OGFM and RGFM approaches, the EGFM simulations demonstrated highly accurate results, where overheating and spurious numerical reflections were completely eliminated in all the cases examined.

The EGFM was extended to 2D flows, and validated against different standard test problems involving interfaces between multiple media. For standard 2D test cases, such as problems with radial symmetry, the EGFM solution consistently reduced interfacial oscillations and unphysical, asymmetrical features resulting from solving such problems on Cartesian meshes. The EGFM was also evaluated in the simulation of a strong shock-interface interaction case with a density ratio of 1000:1, and successfully applied the correct boundary conditions at the interface, while capturing all details of the flow features following the shock-interface interaction. For shock-driven instabilities, the EGFM accurately computed interfacial perturbation growth rates associated with the RM instability in both the linear and nonlinear stages in excellent agreement with a recently proposed nonlinear model [47]. Furthermore, the capability of the EGFM to accurately apply the interfacial boundary conditions associated with surface tension was demonstrated. From our parametric study of the RM instability under the influence of surface tension, we find there is excellent agreement between the simulation results and the analytical model of Mikaelian [54].

In multidimensions, the current implementation of EGFM involves correcting the values at the cells next to the interface. Note that the EGFM algorithm applied on a wider stencil involving cells further from the interface requires the computation of additional source terms (Eq. (18)) that account for the effect of curvature. Since the primary focus of this paper is the solution in the immediate vicinity of the interface (such as flows with surface tension), the performance of EGFM at cells further away, and the improvement through the implementation of the curvature-dependent source terms will be addressed in a future investigation. Nevertheless, we have carefully characterized the accuracy of EGFM for 2D problems, and find the slight overheating errors observed, vanish for $\kappa\Delta x \ll 1$, in contrast to other widely used approaches that were evaluated in this work. Thus, in regions where the local curvature is unusually large relative to the mesh employed, the performance of the

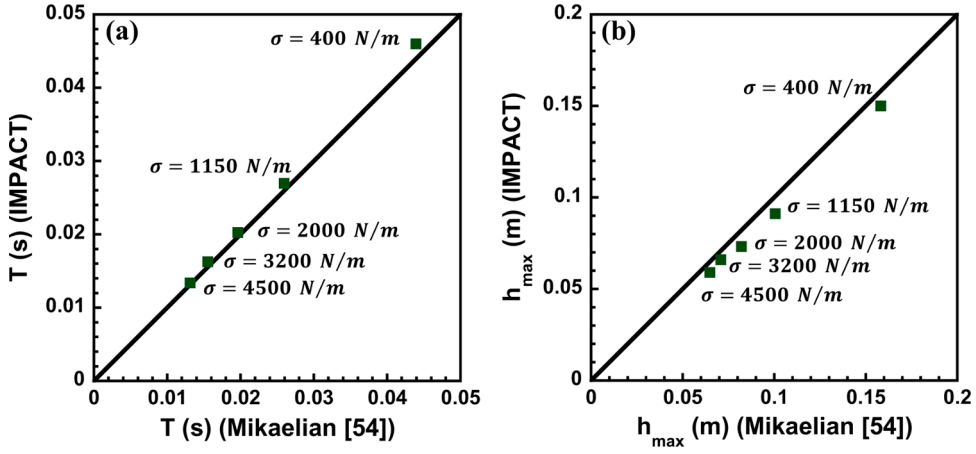

Fig. 21. (a) Period of oscillations and (b) peak amplitude from the RM simulations with different values of the surface tension. The solid black line has a slope of unity and indicates perfect agreement between the IMPACT simulations and the analytical model of Mikaelian [54]. Greater values of σ lead to faster oscillations with lower peak amplitudes.

EGFM will become approximate away from the interface. It is noteworthy that in spite of the approximate implementation, the quality of the 2D solutions were improved as observed in the form of lower overheating errors, removal of oscillations, and precise placement of waves. Another scenario in which the EGFM will be approximate (for both 1D and 2D), is when it is extended to flows governed by equations of state for which the MMRP does not have exact solutions. For such MMRPs involving more general EOS relations, we expect the EGFM to still reduce overheating errors, while not completely eliminating them. A more generalized framework capable of accommodating approximate Riemann solvers will be the focus of future studies.

CRediT authorship contribution statement

Pedram Bigdelou: Conceptualization, Methodology, Software, Validation, Formal analysis, Writing – original draft, Visualization, Investigation, Writing – review & editing. **Chen Liu:** Methodology, Software, Validation, Visualization, Investigation. **Prashant Tarey:** Methodology, Software, Validation, Visualization, Investigation. **Praveen Ramaprabhu:** Conceptualization, Methodology, Writing – review & editing, Supervision, Project administration, Funding acquisition.

Declaration of Competing Interest

The authors declare that they have no known competing financial interests or personal relationships that could have appeared to influence the work reported in this paper.

Acknowledgment

This work was partially supported by the National Science Foundation under Grant No. 1933479.

References

[1] Fedkiw RP, Aslam T, Merriman B, Osher S. A non-oscillatory Eulerian approach to interfaces in multimaterial flows (the Ghost Fluid Method). J Comput Phys 1999;152:457–92. https://doi.org/10.1006/jcph.1999.6236.
[2] Osher S, Fedkiw RP. The level set methods and dynamic implicit surfaces. New York, NY: Springer; 2003. https://doi.org/10.1007/b98879.
[3] Caiden R, Fedkiw RP, Anderson C. A numerical method for two-phase flow consisting of separate compressible and incompressible regions. J Comput Phys 2001;166:1–27. https://doi.org/10.1006/jcph.2000.6624.
[4] Osher S, Sethian JA. Fronts propagating with curvature-dependent speed: algorithms based on Hamilton-Jacobi formulations. J Comput Phys 1988;79:12–49. https://doi.org/10.1016/0021-9991(88)90002-2.
[5] Harvie DJE, Davidson MR, Rudman M. An analysis of parasitic current generation in volume of fluid simulations. Appl Math Model 2006;30:1056–66. https://doi.org/10.1016/j.apm.2005.08.015.
[6] Abgrall R, Karni S. Computations of compressible multifluids. J Comput Phys 2001;169:594–623. https://doi.org/10.1006/jcph.2000.6685.
[7] Shyue KM. An efficient shock-capturing algorithm for compressible multicomponent problems. J Comput Phys 1998;142:208–42. https://doi.org/10.1006/jcph.1998.5930.
[8] Liu TG, Khoo BC, Yeo KS. The simulation of compressible multi-medium flow. I. A new methodology with test applications to 1D gas–gas and gas–water cases. Comput Fluids 2001;30:291–314. https://doi.org/10.1016/S0045-7930(00)00022-0.
[9] Liu TG, Khoo BC, Yeo KS. The simulation of compressible multi-medium flow: II. Applications to 2D underwater shock refraction. Comput Fluids 2001;30:315–37. https://doi.org/10.1016/S0045-7930(00)00021-9.
[10] Cocchi JP, Saurel R. A Riemann problem based method for the resolution of compressible multimaterial flows. J Comput Phys 1997;137:265–98. https://doi.org/10.1006/jcph.1997.5768.
[11] Liu TG, Khoo BC, Yeo KS. Ghost Fluid Method for strong shock impacting on material interface. J Comput Phys 2003;190:651–81. https://doi.org/10.1016/S0021-9991(03)00301-2.
[12] Liu TG, Khoo BC, Wang CW. The Ghost Fluid Method for compressible gas–water simulation. J Comput Phys 2005;204:193–221. https://doi.org/10.1016/j.jcp.2004.10.012.
[13] Wang CW, Liu TG, Khoo BC. A real Ghost Fluid Method for the simulation of multimedium compressible flow. SIAM J Sci Comput 2006;28:278–302. https://doi.org/10.1137/030601363.
[14] Liu TG, Khoo BC. The accuracy of the modified ghost fluid method for gas–gas Riemann problem. Appl Numer Math 2007;57:721–33. https://doi.org/10.1016/j.apnum.2006.07.013.
[15] Xu L, Liu T. Accuracies and conservation errors of various ghost fluid methods for multi-medium Riemann problem. J Comput Phys 2011;230:4975–90. https://doi.org/10.1016/j.jcp.2011.03.021.
[16] Liu TG, Khoo BC, Xie WF. The modified Ghost Fluid Method as applied to extreme fluid-structure interaction in the presence of cavitation. Commun Comput Phys 2006;1:898–919.
[17] Hu XY, Khoo BC. An interface interaction method for compressible multifluids. J Comput Phys 2004;198:35–64. https://doi.org/10.1016/j.jcp.2003.12.018.
[18] Bo W, Liu X, Glimm J, Li X. A robust front tracking method: verification and application to simulation of the primary breakup of a liquid jet. SIAM J Sci Comput 2011;33:1505–24. https://doi.org/10.1137/10079135X.
[19] Hu XY, Khoo BC, Adams NA. A smoothed interface interaction method for compressible flow. In: Proceedings of the 25th international symposium on shock waves; 2005. p. 17–21. July.
[20] Xu L, Feng C, Liu T. Practical techniques in ghost fluid method for compressible multi-medium flows. Commun Comput Phys 2016;20:619–59. https://doi.org/10.4208/cicp.190315.290316a.
[21] Fedkiw RP, Marquina A, Merriman B. An isobaric fix for the overheating problem in multimaterial compressible flows. J Comput Phys 1999;148:545–78. https://doi.org/10.1006/jcph.1998.6129.
[22] Richtmyer RD. Taylor instability in shock acceleration of compressible fluids. Commun Pure Appl Math 1960;13:297–319. https://doi.org/10.1002/cpa.3160130207.
[23] Meshkov EE. Instability of the interface of two gases accelerated by a shock wave. Fluid Dyn 1969;4:101–4. https://doi.org/10.1007/BF01015969.
[24] Bigdelou P. A numerical study of interfacial instabilities in shocked materials with surface tension. ProQuest Dissertations Publishing; 2020, 27959531 [Doctoral dissertation, The University of North Carolina at Charlotte].
[25] Mulder W, Osher S, Sethian JA. Computing interface motion in compressible gas dynamics. J Comput Phys 1992;100:209–28. https://doi.org/10.1016/0021-9991(92)90229-R.
[26] Toro EF. Riemann solvers and numerical methods for fluid dynamics: a practical introduction. Berlin, Heidelberg: Springer; 2009. https://doi.org/10.1007/b79761.
[27] Roe PL. Approximate Riemann solvers, parameter vectors, and difference schemes. J Comput Phys 1981;43:357–72. https://doi.org/10.1016/0021-9991(81)90128-5.
[28] Liu XD, Osher S, Chan T. Weighted essentially non-oscillatory schemes. J Comput Phys 1994;115:200–12. https://doi.org/10.1006/jcph.1994.1187.
[29] Jiang GS, Shu CW. Efficient implementation of weighted ENO schemes. J Comput Phys 1996;126:202–28. https://doi.org/10.1006/jcph.1996.0130.
[30] Zhang R, Zhang M, Shu CW. On the order of accuracy and numerical performance of two classes of finite volume WENO schemes. Commun Comput Phys 2011;9:807–27. https://doi.org/10.4208/cicp.291109.080410s.
[31] Peng D, Merriman B, Osher S, Zhao H, Kang M. A PDE-based fast local level set method. J Comput Phys 1999;155:410–38. https://doi.org/10.1006/jcph.1999.6345.
[32] Min C, Gibou F. A second order accurate level set method on non-graded adaptive cartesian grids. J Comput Phys 2007;225:300–21. https://doi.org/10.1016/j.jcp.2006.11.034.
[33] Shu CW, Osher S. Efficient implementation of essentially non-oscillatory shock-capturing schemes. J Comput Phys 1988;77:439–71. https://doi.org/10.1016/0021-9991(88)90177-5.
[34] Sambasivan SK, UdayKumar HS. Ghost fluid method for strong shock interactions part 1: fluid-fluid interfaces. AIAA J 2009;47:2907–22. https://doi.org/10.2514/1.43148.
[35] Sambasivan SK, UdayKumar HS. Sharp interface simulations with Local Mesh Refinement for multi-material dynamics in strongly shocked flows. Comput Fluids 2010;39:1456–79. https://doi.org/10.1016/j.compfluid.2010.04.014.
[36] Chen H, Liang SM. Flow visualization of shock/water column interactions. Shock Waves 2008;17:309–21. https://doi.org/10.1007/s00193-007-0115-9.
[37] Fechter S, Jaegle F, Schleper V. Exact and approximate Riemann solvers at phase boundaries. Comput Fluids 2013;75:112–26. https://doi.org/10.1016/j.compfluid.2013.01.024.
[38] Liu C. A cut-cell based ghost fluid method for multi-component compressible flows. ProQuest Dissertations Publishing; 2020, 28261447 [Master's thesis, The University of North Carolina at Charlotte].
[39] Shukla RK. Nonlinear preconditioning for efficient and accurate interface capturing in simulation of multicomponent compressible flows. J Comput Phys 2014;276:508–40. https://doi.org/10.1016/j.jcp.2014.07.034.
[40] Nourgaliev RR, Dinh TN, Theofanous TG. Adaptive characteristics-based matching for compressible multifluid dynamics. J Comput Phys 2006;213:500–29. https://doi.org/10.1016/j.jcp.2005.08.028.
[41] Shukla RK, Pantano C, Freund JB. An interface capturing method for the simulation of multi-phase compressible flows. J Comput Phys 2010;229:7411–39. https://doi.org/10.1016/j.jcp.2010.06.025.
[42] Bempedelis N, Ventikos Y. A simplified approach for simulations of multidimensional compressible multicomponent flows: the grid-aligned ghost fluid method. J Comput Phys 2020;405:109129. https://doi.org/10.1016/j.jcp.2019.109129.
[43] Hawker NA, Ventikos Y. Interaction of a strong shockwave with a gas bubble in a liquid medium: a numerical study. J Fluid Mech 2012;701:59–97. https://doi.org/10.1017/jfm.2012.132.

[44] Maxon WC, Nielsen T, Denissen N, Regele JD, McFarland J. A high resolution simulation of a single shock-accelerated particle. J Fluids Eng 2021;143:071403. https://doi.org/10.1115/1.4050007.
[45] Mikaelian KO. Freeze-out and the effect of compressibility in the Richtmyer–Meshkov instability. Phys Fluids 1994;6:356–68. https://doi.org/10.1063/1.868091.
[46] Courant R, Friedrichs KO. Supersonic flow and shock waves. New York: Springer-Verlag; 1976.
[47] Dimonte G, Ramaprabhu P. Simulations and model of the nonlinear Richtmyer–Meshkov instability. Phys Fluids 2010;22:014104. https://doi.org/10.1063/1.3276269.
[48] Dimonte G, Schneider M. Density ratio dependence of Rayleigh–Taylor mixing for sustained and impulsive acceleration histories. Phys Fluids 2000;12:304–21. https://doi.org/10.1063/1.870309.
[49] Alon U, Hecht J, Ofer D, Shvarts D. Power laws and similarity of Rayleigh-Taylor and Richtmyer–Meshkov mixing fronts at all density ratios. Phys Rev Lett 1995;74:534–7. https://doi.org/10.1103/PhysRevLett.74.534.
[50] Thornber B, Griffond J, Poujade O, Attal N, Varshochi H, Bigdelou P, Ramaprabhu P, Olson B, Greenough J, Zhou Y, Schilling O, Garside KA, Williams RJR, Batha CA, Kuchugov PA, Ladonkina ME, Tishkin VF, Zmitrenko NV, Rozanov VB, Youngs DL. Late-time growth rate, mixing, and anisotropy in the multimode narrowband Richtmyer–Meshkov instability: the θ-group collaboration. Phys Fluids 2017;29:105107. https://doi.org/10.1063/1.4993464.
[51] Thornber B, Griffond J, Bigdelou P, Boureima I, Ramaprabhu P, Schilling O, Williams RJR. Turbulent transport and mixing in the multimode narrowband Richtmyer–Meshkov instability. Phys Fluids 2019;31:096105. https://doi.org/10.1063/1.5111681.
[52] Grinstein FF, Saenz JA, Germano M. Coarse grained simulations of shock-driven turbulent material mixing. Phys Fluids 2021;33:035131. https://doi.org/10.1063/5.0039525.
[53] Grinstein FF, Pereira FS. Impact of numerical hydrodynamics in turbulent mixing transition simulations. Phys Fluids 2021;33:035126. https://doi.org/10.1063/5.0034983.
[54] Mikaelian KO. Rayleigh-Taylor and Richtmyer–Meshkov instabilities in multilayer fluids with surface tension. Phys Rev A 1990;42:7211–25. https://doi.org/10.1103/PhysRevA.42.7211.
[55] Garrick DP, Owkes M, Regele JD. A finite-volume HLLC-based scheme for compressible interfacial flows with surface tension. J Comput Phys 2017;339:46–67. https://doi.org/10.1016/j.jcp.2017.03.007.